

Electronic Thesis and Dissertation Repository

1-30-2013 12:00 AM

Atlas-Based Attenuation Correction for PET/MRI

John Christian Patrick, *The University of Western Ontario*

Supervisor: Dr. Robert Stodlika, *The University of Western Ontario*

A thesis submitted in partial fulfillment of the requirements for the Master of Science degree in Medical Biophysics

© John Christian Patrick 2013

Follow this and additional works at: <https://ir.lib.uwo.ca/etd>



Part of the [Medical Biophysics Commons](#)

Recommended Citation

Patrick, John Christian, "Atlas-Based Attenuation Correction for PET/MRI" (2013). *Electronic Thesis and Dissertation Repository*. 1143.

<https://ir.lib.uwo.ca/etd/1143>

This Dissertation/Thesis is brought to you for free and open access by Scholarship@Western. It has been accepted for inclusion in Electronic Thesis and Dissertation Repository by an authorized administrator of Scholarship@Western. For more information, please contact wlsadmin@uwo.ca.

ATLAS-BASED ATTENUATION CORRECTION FOR PET/MRI

by

John Christian Patrick

Graduate Program in Medical Biophysics

A thesis submitted in partial fulfillment
of the requirements for the degree of
Master of Science

The School of Graduate and Postdoctoral Studies
The University of Western Ontario
London, Ontario, Canada

© John C. Patrick 2013

Abstract

Attenuation correction (AC) in PET/MRI is difficult as there is no clear relationship between MR signal and 511 keV attenuation coefficients (μ). One strategy is to align a pre-defined atlas of μ to the PET/MRI for AC. However, atlas design may influence quantitative accuracy of AC. In this thesis we compare 3 atlas design strategies and evaluate their performance in an oncology patient population. The 3 strategies were: correction with BMI-dependent atlases; gender-dependent atlases, and a gender- and sex-independent atlas. Patients were imaged with FDG PET/CT and 3T MRI. The atlases were created and then used for PET AC of patients not included in the atlas construction. Resulting PET images were compared to CT-based PET reconstructions across all voxels and tissue-specific volumes. For the purposes of AC, there is value in developing specialized atlases. To this end, gender plays a more important role than body mass index in atlas construction.

Keywords

Hybrid, Attenuation Correction, PET/MRI, Atlas, Gender, BMI

Co-Authorship Statement

Chapter 2 was co-authored by Dr. Harry Marshall, Dr. Frank Prato, Mr. John Butler, Dr. Jean Théberge, Dr. Terry Thompson, and Dr. Robert Stodilka. Dr. Stodilka helped conceive, formalize, and develop the ideas. Drs. Stodilka and Marshall assisted in experimental design and data analysis. Dr. Marshall and Mr. Butler partook in data collection. Drs. Stodilka, Théberge, Thompson, Prato, and Marshall critically reviewed the manuscript. I was involved in the conception of the idea, experimental design, and data collection. I constructed the atlases and related code as necessary, performed the data analysis and wrote the related code, as well as wrote the manuscript.

Acknowledgments

I would like to start by thanking my supervisor Dr. Robert Stodilka for his guidance and enthusiasm throughout my masters. As a mentor he has taken a genuine interest in getting to know me, my goals, as well as my strengths and areas to improve. He has provided me with ample information, opportunity, and insight drawn from his personal experiences to help me refine my goals and better prepare me for challenges ahead. I consider myself to be very fortunate to have had the opportunity to study under his supervision.

I would also like to thank my advisory committee members, Dr. Frank Prato, Dr. Jean Théberge, and Dr. Terry Thompson. Regardless of how busy he was, Dr. Prato's office door has always been open and he has always made time to answer any question I've had with a smile. He has always been encouraging and a genuine pleasure to work for and with and I look forward to working together with him again. Dr. Théberge was always there to answer my questions and provide many insights. His expertise and generosity with information and time was greatly appreciated. Dr. Thompson not only made his time available whenever I needed it, but he also presented me with a variety of great opportunities here at Lawson which were key to getting me to where I am today. I cannot say thanks enough for everything you have all done for me. You have all taught me the value of perseverance and I am a better person for it.

Although he did not sit on my advisory committee, Dr. Alex Thomas has played an important role in providing guidance and insight. He has been, and continues to be, a great mentor. Thank you for your advice, many lessons, and planting the thought of graduate school in my head by repeatedly asking, "When are you going to start your PhD?" back when I was working on my undergrad. I now have an answer for him; "Now".

These experiments would not have been possible without John Butler and his technical knowledge of operating the MRI. Also, John's pleasant and professional rapport with patients notably instilled confidence. It was his ability to put people at ease that helped with patient recruitment. In the same way, the PET/CT data would not have

been possible without the nuclear medicine techs, Don Kuhl, Ben Reyes, Karen Keys, Peter Masters, Gina Iacbelli, Jessica Wall, and Paul Sery. They were always a joy to work with and were very helpful in answering my many questions. In the process of patient recruitment, making sure that each patient has all of the necessary information beforehand is crucial. This recruitment would not have been possible and I would not have been able to enroll these patients without the help of Lindsay Douglas and Tracy Zurbrigg. Lindsay, thank you for organizing and mailing out the letters of intent and ensuring that patients had plenty of time to review the information before they arrived. Tracy, thank you for keeping me in the loop for patient arrival times, names, and for allowing me to loiter in your office chair next to you, as I waited for them to arrive.

I would like to thank my lab members, Dr. Eric Sabondjian and Dr. Harry Marshall. Eric, being a first-rate friend and my first office mate, showed me the ropes as a graduate student. He has been a constant source of encouragement and help. Ninja, Trailblazer, and now future Brother-in-law, I look forward to seeing you at many future family gatherings to come. Harry, thank you for all of your instruction on the ins and outs of MRI-based attenuation correction. You have been an invaluable source of information and comedy. Our office meetings were always insightful and entertaining.

I would also like to acknowledge our wonderful Lawson Imaging Administrative Staff. Brenda Dubois, Michele Avon, and Shelagh Ross were always very helpful with any administrative needs and did so with a smile. They have been an integral part to many of my successes at Lawson Imaging as well as friends to many of us. Thank you!

Last but definitely not least, I would like to thank those closest to me. Thank you to my girlfriend Lindsay Douglas, who has believed in me and supported me through all of the good and bad times over the past 3 years. To my little sister Susan Patrick, thank you for always cheering me on and looking out for me. To my parents Nancy and Roy Patrick, thank you for your unconditional love and support through the years. Thank you for lifting me up when I was down and bringing me back down to earth when my head was in the clouds. I love you all.

Table of Contents

Abstract.....	ii
Co-Authorship Statement.....	iii
Acknowledgments.....	iv
Table of Contents	vi
List of Tables	ix
List of Figures	x
List of Appendices	xii
Nomenclature	xiii
Chapter 1	1
1 Oncology Imaging in General.....	1
1.1 X-ray Computed Tomography (CT).....	1
1.2 Magnetic Resonance Imaging (MRI).....	2
1.3 Nuclear Medicine Imaging	5
1.3.1 SPECT.....	6
1.3.2 PET in Oncology.....	7
1.3.3 ¹⁸ F-fluorodeoxyglucose (FDG).....	9
1.3.4 Positron Emission Tomography – The Scanner.....	11
1.4 Challenges with Quantification.....	13
1.4.1 Detector Normalization.....	13
1.4.2 Random Coincidence Correction	14
1.4.3 Scatter Correction	16
1.4.4 Attenuation Correction.....	17

1.5 Attenuation Correction Methods.....	18
1.5.1 Non-Transmission μ -maps.....	18
1.5.2 Transmission-based μ -maps	19
1.5.2.1 Radionuclide Transmission Scans.....	19
1.5.2.2 X-ray CT Scans	20
1.5.2.3 PET/MRI	21
References.....	25
Chapter 2.....	34
2 A Comparison of Gender and BMI-based approaches to Atlas Design for Attenuation Correction in PET/MRI.....	34
2.1 Introduction.....	34
2.1.1 Image Segmentation.....	34
2.1.2 Mapping	35
2.1.3 Atlas Map Registration	36
2.2 Methods.....	37
2.2.1 Data Preparation and Preprocessing	39
2.2.2 Atlas Construction	39
2.2.3 Correcting for Attenuation in Patient Data with Atlases	40
2.2.4 Data Analysis	43
2.3 Results.....	43
2.4 Registration.....	49
2.5 Discussion	51
2.6 Conclusion	54
References.....	56
Chapter 3.....	58

3.1 Summary	58
3.2 Future Directions and Limitations	59
3.3 Conclusion	63
References.....	64
Curriculum Vitae	68

List of Tables

Table 2-1: Summary of parameters from LOBF in global analysis.....	45
Table 2-2: : Mean relative percent errors and standard deviations for corrections made with each of the three atlas design methods.....	55

List of Figures

Figure 1-1: Cyclotron - Positive ions created inside are accelerated between the hollow electrode chambers (Dees) by a square wave electric field, which reverses just as the ions approach the gap. The ion path spirals away from the center, perpendicular to the field direction until they collide with the target.	9
Figure 1-2: 2-Deoxy-2-(¹⁸ F) Fluoro-D-Glucose	10
Figure 1-3: A schematic comparison of metabolic pathways between glucose and ¹⁸ F-fluorodeoxyglucose (¹⁸ F-FDG) through a cell membrane.	11
Figure 1-4: A schematic diagram of rings of gamma detectors of a PET scanner. The inset schematically shows an example of a detector block configuration.	12
Figure 1-5: A schematic showing a Line of Response (LoR) from a random coincidence event.	15
Figure 1-6: A schematic showing a Line of Response (LoR) from a scatter coincidence event.	16
Figure 2-1: Atlas-based Reconstruction Comparison: A) A standard PET reconstruction for comparison. The CT image is converted into a mapping of attenuation values. This is then used to correct for the attenuation in the PET image. B) In our Atlas-based approach, the MRI component of the atlas is registered to the patient's MRI. The transformations used to register these MR images are then applied to the CTAC component of the Atlas. This registered CTAC is then used to correct for attenuation in the patient PET. C) We then compare the Atlas-based Corrected PETs to the standard CT corrected PET.	42
Figure 2-2: Coronal μ -map images. A) A single CTAC. B) An averaged Normal BMI atlas. C) An averaged overweight BMI atlas. D) An averaged obese BMI atlas. E) An averaged male atlas. F) An averaged female atlas. G) An averaged fully amalgamated atlas	44

Figure 2-3: Mean relative percent error for VOIs from PET images corrected with each approach. Error bars indicating standard deviations for each category.46

Figure 2-4: Scatter plot of Overweight BMI-based atlas corrected PET versus CTAC reconstructed PET (Patient 12)47

Figure 2-5a: Intensity profiles through a CTAC reconstructed PET (orange) and a Male Gender-based atlas reconstructed PET (blue) for Patient 12. 53

List of Appendices

Appendix A: Ethics Approvals.....	66
-----------------------------------	----

Nomenclature

μ	Linear Attenuation Coefficient
3D	Three-Dimensional
3T	3 Tesla
4D	Four-Dimensional
AC	Attenuation Correction
ADC	Apparent Diffusion Coefficient
APD	Avalanche Photodiodes
B_0	Main magnetic field strength of the MR scanner
BGO	Bismuth Germanium Oxide
BMI	Body Mass Index
CT	Computed Tomography
CTAC	CT-based attenuation correction
DWI	Diffusion Weighted Imaging
FDG	^{18}F -fluorodeoxyglucose
FoV	Field of View
LOBF	Line of Best Fit
LoR	Line of Response
LSO	Lutetium Oxyorthosilicate
m	Slope of LOBF
MRI	Magnetic Resonance Imaging
NSCLC	Non-Small Cell Lung Cancer
p	Probability of a type-1 error
PET	Positron Emission Tomography
PMT	Photomultiplier Tubes
R^2	Pearson product-moment correlation coefficient
RF	Radio Frequency
S.D.	Standard Deviation
SLN	Sentinel Lymph Node
SNR	Signal-to-Noise Ratio

SPECT	Single Photon Emission Computed Tomography
SPN	Solitary Pulmonary Nodule
SUV	Standardized Uptake Values
T1	Spin-lattice relaxation time
T2	Spin-spin relaxation time
T2*	Spin-spin relaxation time with local magnetic field inhomogeneities
TE	Echo Time
TR	Repetition Time
USPIO	Ultra Small Particle Iron Oxide
UTE	Ultra-Short Echo
VOI	Volume of Interest
ω	Precessional frequency of protons
γ	Gyromagnetic ratio

Chapter 1

1 Oncology Imaging in General

Medical imaging is an integral component of comprehensive cancer care, whether looking at biological or pathological processes. It provides us with many benefits, which include minimal to no invasiveness, real time monitoring, and can provide us with valuable information over wide ranges of time and size scales (1).

The importance of medical imaging is constantly growing in all aspects of cancer care (2, 3). Some of the ways we are seeing medical imaging contribute include aiding with prediction (4), screening patients (5), preoperative staging (6), planning therapy (7), therapy guidance (8), and seeing how patients respond to therapy (9, 10). Some of the modalities that have been instrumental in this progress include X-ray Computed Tomography (CT), Magnetic Resonance Imaging (MRI), Single Photon Emission Computed Tomography (SPECT) and Positron Emission Tomography (PET); and more recently examples have emerged of multiple modalities being coupled together in so-called “hybrid” modalities.

1.1 X-ray Computed Tomography (CT)

X-ray CT is among the most important of imaging technologies in cancer diagnosis and staging, and plays many roles. For example, CT can be used for virtual colonography (11), providing information about colon tumors themselves as well as metastases in the lymph nodes and the liver (12, 13). X-ray CT is also frequently used to guide interventional procedures. Some of these include guided brachytherapy (14, 15), radiofrequency ablation of hepatic metastases and hepatocellular carcinoma (16), renal tumours (17), and of bone metastases (18), as well as transcatheter arterial chemoembolization (19), and guided biopsies (20-22).

In recent years, there is a growing trend of using X-ray CT for whole-body screening; however this application has received mixed opinions. For example, in a large study of 1192 patients, 14% of scans were completely negative for any findings. Of the remaining

86%, only 4% had a previous medical history reported. The majority of findings were benign, and 37% were recommended for additional evaluation (23). With so many of these findings being benign or requiring additional evaluation, one might question if there is a more efficient and lower risk modality for performing whole-body screening.

Conversely, some progress has been made to reduce dose in X-ray CT scanning. Recently, iterative reconstruction algorithms, originally developed for high-noise nuclear medicine tomographic applications, have been ported to CT. These methods allow radiation dose in CT scanning to be reduced without sacrificing image quality. Various iterative reconstruction techniques have seen dose reductions from 25-65% (24-26).

X-ray CT has also seen a growing convergence with radiotherapy treatment planning (27-29), which has promoted the use of larger x-ray detectors and higher power x-ray tubes. These developments, along with temporal gating of scanning ("4D" scanning) has improved the usefulness of CT for tumour tracking at every point throughout the breathing cycle. Combining this with Intensity Modulated Radiotherapy, an advanced type of high-precision radiation therapy that also relies upon temporal gating, improves the ability to deliver efficacious therapeutic radiation doses to the tumor site while sparing surrounding tissue (30).

1.2 Magnetic Resonance Imaging (MRI)

MRI is among the most flexible of imaging modalities in terms of its ability to derive a multitude of contrasts from both endogenous tissue properties, as well as detect the presence of exogenous contrast agents introduced into the body.

The majority of clinical MRI relies on signal derived from the hydrogen nuclei. The hydrogen nuclei consist of a single proton and, therefore, have a net magnetic moment and spin of $1/2$. Hydrogen nuclei are most abundant in tissue, water and lipids and act like microscopic bar magnets rotating along their longitudinal axis. Typically, the magnetic moments of hydrogen protons within a sample are oriented in random directions, resulting in no net magnetization of the sample at the macroscopic level. However, when the sample is placed within a strong static magnetic field, the protons

will start to precess about the orientation of the static field. The proton will then be in a mixed energy state composed of two eigenstates referring to the direction of the longitudinal component of the proton's magnetic moment: the parallel state and the antiparallel state. Over a brief period of time, energy exchange with the surrounding lattice through thermodynamic processes (rotations and vibrations) will result in a slight excess of protons in the parallel state (i.e. lower energy state). This will result in the acquisition of a net macroscopic magnetization by the sample in the direction of the MR's static field. This net magnetization is where we derive our signal to produce our image. The frequency of the proton's precession is determined from the Larmor equation:

$$\omega = \gamma B_0$$

where γ is the gyromagnetic ratio, which is equal to 42.6 MHz/T and B_0 is the main magnetic field strength of the MR scanner. In order to exploit resonant absorption of the MR transmitted RF electromagnetic field, the frequency must be selected to match at the precessional frequency of the protons, which is calculated via the Larmor equation. The RF field produces a new effective direction of the magnetic field experienced by the protons and they will start to precess around this direction, resulting in the net magnetization rotating away from the longitudinal direction of the main field. The amount of rotation, or the *flip angle*, depends on the strength and duration of the RF pulse. A flip angle of 90° will maximize the amount of transverse magnetization produced. This is important as only the transverse component of the magnetization will induce a detectable signal in the MRI receiver coil. The same inter-molecular interactions that allowed the formation of the macroscopic magnetization, T1 processes, will force the return of the magnetization to its equilibrium state along the direction of the main field. The rate at which the magnetization returns to the longitudinal axis is different for protons in different tissues. It is this tissue-specific variation in the rate of its magnetization's return to equilibrium which provides the fundamental source of contrast in T1-weighted images.

T2 is a parameter that characterizes the rate of dephasing, or loss of coherence, of the protons associated with a given tissue. Transverse relaxation begins with the net magnetization aligned perpendicular to the direction of the main field. As spins experience random field fluctuations due to the field produced by the movement of neighboring spins, the phase of the individual spins forming the macroscopic magnetization progressively loses coherence and the resulting magnitude of the vector sum diminishes exponentially with time. Different tissues have different T2 values due to their different molecular composition and therefore, T2 decay is another source of contrast in MRI.

Echo Time (TE) is the time between the peak of the excitation RF pulse and the peak of the echo that is formed from rephasing of the spins. Repetition Time (TR) is the time that it takes to run through the pulse sequence once. The pulse sequence typically needs to be repeated 256 times to construct an image with 256 lines. TE and TR can be used to control the amount of “weighting” of these T1 and T2 effects in our image. A change in TR will control the amount of T1-weighting and a change in TE will control the amount of T2-weighting.

Many MRI-based methods can be applied to cancer detection and staging, evaluation of therapeutic response and even biopsy guidance. Herein, our literature survey will list only a few examples meant to illustrate the flexibility of MRI.

An application of MRI that is growing rapidly in profile is breast imaging. Breast MR imaging is very important for staging because of its ability to show multi-focal tumours, involvement of other anatomy, and presence of metastases. MRI has been shown to be superior to ultrasound and mammography for assessing pathological response to treatment and a low rate of re-operation (9.5%) for positive margins after breast conserving surgery (31). This makes MRI an important tool in aiding clinical decision-making between breast-conserving surgery versus mastectomy.

Another area receiving increased attention for oncological applications is MRI Diffusion Weighted Imaging (DWI), a method in which the MRI contrast is dependent on the ability of water molecules to diffuse freely within the tissue. This has utility in cancer

imaging because tumour tissue tends to feature microstructural abnormalities that affect the diffusion of water molecules and lower the apparent diffusion coefficient (ADC). This allows the tumors to be detected as bright signals on diffusion-weighted images and signal voids on ADC maps. DWI is also useful in monitoring therapeutic response since observed increases in ADC following therapy are thought to result from cellular water being freed into the extracellular space following cancer cell death (32). Therefore, a positive response to therapy is indicated by a rise in ADC. An example of this can be seen with changes in hepatic metastases from neuroendocrine tumours following transarterial chemoembolization imaged with DWI MRI of the liver (33).

As with many medical imaging modalities, MRI images can rely upon either endogenous contrast or exogenous contrast agents introduced into the body. There are many examples of the latter; however, one exogenous contrast agent that has been attracting considerable attention recently is Ultra Small Particle Iron Oxide (USPIO). Accumulation of this contrast agent causes a sharp reduction (loss) in an MR imaging parameter known as T2*. An example of USPIO application is in the detection of lymph node involvement in the spread of cancer from a primary tumor site. In many cases, diseased lymph nodes become enlarged, relative to their healthy counterparts – making the diseased nodes easy to detect. However, diseased nodes, which are not enlarged become difficult to detect. In a recent study, combining USPIO MRI and a different imaging modality - Positron Emission Tomography using the 18F-based radiotracer fluorodeoxyglucose - achieved 100% sensitivity, specificity, positive predictive value, and negative predictive value in diseased lymph node detection in breast imaging, as confirmed by histopathology (34). Further to this success, USPIO MRI is also receiving attention in evaluating lymph node involvement with prostate, colorectal cancer and lung cancer.

1.3 Nuclear Medicine Imaging

Nuclear medicine modalities consist of Single Photon Emission Computed Tomography (SPECT) and Positron Emission Tomography (PET). Unlike X-ray Computed Tomography and Magnetic Resonance Imaging, the nuclear medicine modalities do not image endogenous contrast. However, their ability to detect their associated gamma-ray

emitting exogenous contrast agents remains far unchallenged. SPECT, and moreso PET, are capable of detecting contrast agents in the nanomole/kg and picomole/kg concentrations. In comparison, X-ray CT has sensitivities of a few millimole/kg, while MRI sensitivity has been reported to be approximately 10 millimole/kg (1). The high sensitivity of nuclear medicine modalities allows the use of relatively little exogenous contrast and the benefit of having an exceedingly low rate of pharmacological reaction (1).

In both SPECT and PET, the exogenous contrast agent is referred to as a radiotracer. It is comprised of a radioactive atom that emits gamma-rays upon its radioactive decay; and a molecule that has biological relevance. The biological relevance can include affinity to certain types of cells, or properties that facilitate or prevent diffusion across a membrane. In general, these radiotracer properties allow detection of cell populations, measurement of filtration or blood flow, and, by extension, the differentiation of diseased tissues from healthy tissues. In many cases, abnormal tracer uptake can be indicative of disease processes such as cancer (35) or tissue damage, as would be the case following a heart attack (36). SPECT and PET are often referred to as *functional* imaging modalities, since they show tissue health, rather than anatomical structure. SPECT and PET differ in that the latter relies upon the detection of *pairs* of gamma-rays, in contrast to *Single Photon Emission Computed Tomography*.

Both SPECT and PET have a multitude of uses in oncology. For SPECT, we will survey two examples that have received increased attention in recent reports. We will then turn our attention to PET, where exciting applications are growing at an exponential rate.

1.3.1 SPECT

A long-standing, but growing, application of oncologic SPECT is in the identification of the Sentinel Lymph Node (SLN), which is the first lymph node met by lymphatic vessels draining a tumour (37). The absence of tumour cells in the SLN could indicate the absence of metastatic disease in other surrounding nodes. If the SLN is identified and found to contain no tumour cells, extensive node dissection surgery can be avoided.

Lymph node drainage patterns can be seen by SPECT using ^{99m}Tc -labelled human serum albumin (38, 39). In a review of 14 articles on the role of SPECT/CT – a form of SPECT that is combined with X-ray CT – in the preoperative detection of sentinel lymph nodes in breast cancer (40), the authors found that SPECT/CT improved both identification and staging of breast cancer when compared with planar lymphoscintigrams.

SPECT has, and continues to, see roles in pharmaceutical development, where radiotracer versions of therapeutic drugs are used to measure pharmacokinetics and identify the ultimate fate of the drug. Here, SPECT has accelerated drug development and minimized the effort spent on ineffective treatments for cancer patients (41). An example of this can be seen with the use of folate-targeted imaging agents to predict response to therapy with folate-targeted therapy in advanced ovarian cancer (42). In this study it was suggested that use of folate receptor targeted EC20 (a ^{99m}Tc -labeled imaging agent) imaging can identify patients with advanced ovarian cancer who are most likely to benefit from therapy with folate receptor targeted EC145.

1.3.2 PET in Oncology

PET, like SPECT, seeks to measure the distribution of an administered radiotracer. In the case of radiotracers designed for PET, however, the radioactive atoms on the tracers do not themselves emit gamma-rays. Instead, they decay (often but not always) by emitting a positron – the anti-matter counterpart to the electron. This positron travels a certain distance, determined by its kinetic energy, and then interacts with an electron in mutual annihilation, leading to the emission of two 511 keV gamma-rays in nearly opposite directions. The PET scanner detects these two gamma-rays in near time-coincidence. By repeatedly detecting these events, the PET scanner is able to measure projections of the distribution of the administered radiotracer. Then, using the principles of computed tomography, similar to those found in SPECT and X-ray CT, these projections are combined to create a three-dimensional representation of the radiotracer distribution in the body.

PET has seen broad applications in oncology, cardiology and neurology. It features a number of advantages over its single photon counterpart: more flexible radiochemistry

which allows a greater selection of radiotracers to be developed, shorter half-lives of radionuclides simplifying repeat studies in individuals, and increased sensitivity to low concentrations of radiotracers. However, PET has always been more expensive than SPECT, which contributed to its smaller deployment historically.

However, in the 1990s, an important invention was made that would change PET – and many imaging modalities – forever: the hybridization of imaging modalities. A PET scanner was combined with an X-ray CT scanner, leading to PET/CT (Patent No: US 6,490,476 B1; Townsend, D.W et al, Nuclear Science Symposium, 1998. Conference Record. 1998 IEEE). Now, for the first time, the exquisite biological information made available via visualizing radiotracer distribution was combined with the anatomical referencing made possible with X-ray CT. This is in part why PET/CT has become such a powerful tool for the detection of cancer. For example, in conjunction with the radiotracer ^{18}F -FDG, the sensitivity of PET/CT aids in the early detection of tumours, allowing for early treatment (43) and its high specificity aids in the identification of non-specific benign lesions (44, 45). In tumor staging: FDG-PET has been found to be more accurate than CT in staging disease in the mediastinum in patients with lung cancer (46). Further still, integrated FDG-PET/CT has been found to be even better at predicting stage I and II disease as well as size of the tumor and whether it has invaded nearby tissue (T) and regional lymph nodes that are involved (N), of patients with non-small cell lung cancer (NSCLC) when compared with dedicated PET alone. There were similar findings in a study of 27 patients with lymphoma, which concluded that FDG-PET/CT imaging was accurate in re-staging lymphoma and offered advantages over separate FDG-PET and CT imaging (47). In the same way that SPECT can be used to assess cancer response to a therapeutic prescription to determine efficacy early on during treatment, PET can be used for follow-up scans to detect progressive disease or recurrence. Van Loon et al (2009) found that PET-scanning after curative treatment for NSCLC led to the detection of progression, and that selectively offering a PET/CT scan to the patients without symptoms could possibly lead to an effective follow-up method (48).

Also, like SPECT radiotracers, drugs can be labelled with a radionuclide without changing the drug's biochemical properties. This makes it possible to use trace quantities

of a drug to predict its pharmacokinetics and distribution at therapeutic quantities with less probability for unintended reactions. Various radiolabeled chemotherapy agents have been studied, such as [^{18}F]tamoxifen (49), [^{18}F]fluorouracil (50), and [^{18}F]paclitaxel (51).

1.3.3 ^{18}F -fluorodeoxyglucose (FDG)

Of the many potential radioisotope tracers that could be used in PET imaging, FDG is one that has proven most useful particularly in oncology imaging. FDG is a molecule that is very similar to glucose, and shares many – but not all – of its biochemical traits.

FDG is labeled with the radionuclide ^{18}F . A popular method for producing ^{18}F is in a medical cyclotron. A cyclotron is a particle accelerator used to accelerate charged particles outwards from the center along a spiral path (Figure 1-1).

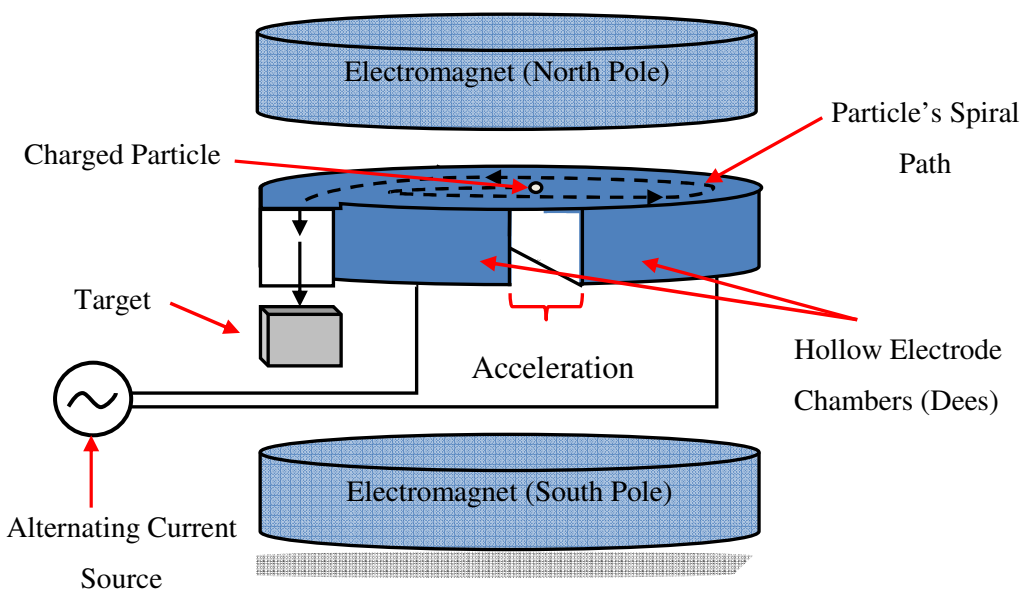
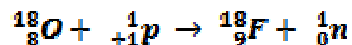


Figure 1-1: Cyclotron - Positive ions created inside are accelerated between the hollow electrode chambers (Dees) by a square wave electric field, which reverses just as the ions approach the gap. The ion path spirals away from the center, perpendicular to the field direction until they collide with the target.

A static magnetic field holds the particles to the spiral path and they are accelerated by a rapidly varying electric field. In the case of ^{18}F , the cyclotron is used to bombard ^{18}O

atoms (chemically present as ^{18}O enriched water) with high energy protons, resulting in the reaction:



The FDG molecule itself differs from glucose in that the ^{18}F substitutes for a hydroxyl group in the 2' position, as shown in Figure 1-2.

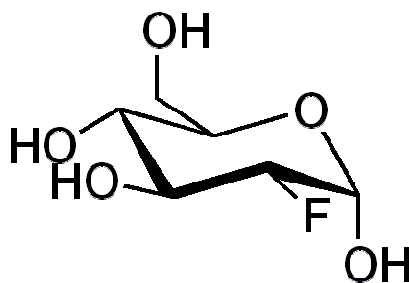
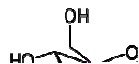


Figure 1-2: 2-Deoxy-2-(^{18}F) Fluoro-D-Glucose

In the body, glucose is central to the production of metabolic energy. Typically, after glucose is consumed by an individual, it becomes distributed in the blood, and is taken up by cells via membrane-bound glucose transport proteins (See Figure 1-3). Inside the body's cells, glucose interacts with an enzyme known as hexokinase, and becomes phosphorylated, forming glucose-6-phosphate. This new molecule then reacts with glucose-6-isomerase to form fructose-6-phosphate, and finally enters the Krebs cycle.

FDG, like glucose, enters the cell via membrane transport proteins; and then undergoes phosphorylation by hexokinase. However, the resulting FDG-6-phosphate cannot interact with glucose-6-isomerase, and hence does not proceed to the Krebs cycle. Instead, FDG-6-phosphate merely accumulates in the cell – where it ultimately serves as an indicator of glycolytic activity. This feature of FDG makes it extremely useful in oncology since glycolysis is greater in many tumour cells than in their healthy counterparts (52). In general, the increased FDG observed in cancerous tissue is due to upregulated activities of glucose transporters (GLUT1 and GLUT3) and hexokinases (I and II) (53, 54). Although glycolytic rate can be regulated at many different steps in the

glycolytic pathway (55, 56), the majority of studies on this process in cancer suggest that control over glycolytic flux is found at the transport and phosphorylation level (57-59). As a result, FDG accumulates in cells with high metabolic activity.



1.3.4 Positron Emission Tomography – The Scanner

A PET scanner is physically arranged as a ring, or multiple rings stacked axially, of detection elements surrounding the region to be imaged (See Figure 1-4). The rings are comprised of circumferentially placed *block detectors* facing inwards. The block detector itself consists of an inorganic scintillation crystal and a square array of photomultiplier tubes (PMTs), and is in essence a miniature version of the gamma camera that is used in SPECT imaging.

The role of the scintillation crystal is to absorb, via the photoelectric process, incoming gamma-rays and convert them into an optical fluorescent signal that is detectable by the PMT array. Considerable effort has been placed into the development of

scintillation crystals. Until the late 1990's the near-ubiquitous choice of crystal was Bismuth Germanium Oxide ($\text{Bi}_4\text{Ge}_3\text{O}_{12}$, or simply BGO), which provided excellent traits for detection of 511 keV gamma-rays. More recently, however, BGO is being supplanted by lutetium oxyorthosilicate (Lu_2SiO_5 , or LSO), which features superior gamma-ray count rate capability, but has the disadvantage of being slightly radioactive (featuring a beta decay of natural ^{176}Lu).

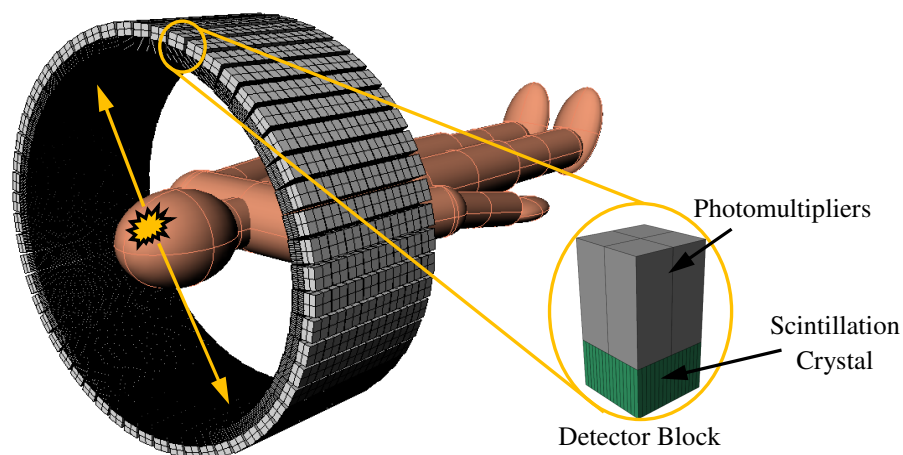


Figure 1-4: A schematic diagram of rings of gamma detectors of a PET scanner. The inset schematically shows an example of a detector block configuration.

Behind the scintillation crystal is an array of PMTs. A PMT is a type of vacuum tube that is extremely sensitive to light detection (in the near-ultraviolet to near-infrared range of the electromagnetic spectrum). A PMT uses a sequentially-arranged series of dynodes to multiply the current produced by incident light many millions of times, enabling the detection of even individual photons.

The PMTs are spatially arranged behind the scintillation crystals to detect fluorescent light output following the absorption of a gamma-ray, where PMTs closer to the gamma-ray absorption will receive more light signal. Each PMT is connected to electronic circuitry to reflect the relative amount of light sensed by the array. When a gamma-ray impinges on the scintillation crystal, all PMTs detect simultaneously the same flash of

light to varying degrees, depending on their spatial position from the individual event. Thus the spatial location of each “flash” of light in the scintillation crystal is reflected as a pattern of signals within the interconnecting array. The pattern of signals, specifically the relative amount of light from each PMT, is then interpreted by a computer to identify the location of the scintillation event in the crystal. The summation of all signals from the PMT array is proportional to the total energy of the absorbed gamma-ray.

Since it is known *a priori* that PET radiotracers emit 511 keV gamma-rays in opposite directions but simultaneously, the PET scanner purposefully seeks gamma-rays being detected in near time-coincidence (with an acceptance window of typically 6 to 12 nanoseconds). If two gamma-rays are registered as coincident, it becomes possible to identify their point of origin as being along a line joining the spatial locations of the detection events. This line is termed a line-of-response (LoR). By measuring hundreds of thousands of detection events along different LoRs, the resulting data can be sorted into projections of the distribution of the radiotracer inside the body. These projections can then be reconstructed using various algorithms into three-dimensional tomographic maps of the radiotracer distribution.

1.4 Challenges with Quantification

PET, even more than SPECT, has focused on quantification and quantitative accuracy. This was driven mostly by the role of PET being restricted, before PET/CT, to academic centres. However, quantification is not straightforward, as detecting and positioning gamma-rays is compromised by the physical processes of scatter and attenuation; whereas, the PET scanner itself is bound by limitations in gamma-ray count rate capabilities, and position detecting of gamma-rays. These phenomena must be accounted for, and broadly speaking this is accomplished by way of detector normalization, and corrections for random coincidences, and scattered and attenuated gamma-rays. We will describe each in turn.

1.4.1 Detector Normalization

PET scanners are comprised of hundreds of individually-cut scintillation crystals. Each of these crystals can have slight variations in dimensions, and quality of optical coupling

between the crystal and the underlying PMT array. Hence, the efficiency of the conversion of gamma-ray energy to an electrical signal varies between block detectors. These differences lead to variations in sensitivity and resolution across the field of view (FoV). Correcting for these variations to achieve uniformity is termed normalization.

One approach to normalizing detectors is to record the number of counts detected by each coincidence pair of detectors during exposure to a uniform radionuclide source. With the radionuclide source extended through the axial FoV and rotating it around the periphery once, all detector pairs are exposed to the same number of gamma-ray pairs. As some detector pairs will record more counts and some will record fewer counts, the normalization factor for each detector pair (a,b) is calculated from ,

$$\mathbf{NormFactor}_{(a,b)} = \mathbf{Counts}_{(a,b)} / \mathbf{AvgCt},$$

where $Counts_{(a,b)}$ is the number of counts for detector a and b , and $AvgCt$ is the average counts for all detector pairs. This can then be used to correct the number of counts for each detector pair by,

$$\mathbf{Corrected}_{(a,b)} = \mathbf{NewCounts}_{(a,b)} / \mathbf{NormFactor}_{(a,b)}$$

where $NewCounts_{(a,b)}$ is the uncorrected count number for a patient scan. This is applied to the projection data before proceeding to tomographic reconstruction.

1.4.2 Random Coincidence Correction

A random coincidence occurs when two unrelated positron annihilation events occur simultaneously, and a single gamma-ray from each of those events is detected in time coincidence and then erroneously paired along a LoR (Figure 1-5). The net effect of such random coincidences is to add a relatively uniform background of counts across the FoV, ultimately suppressing image contrast and distorting the relationship between the true concentration of radiotracer in a location compared with its measured amount.

A very popular method for correcting the effect of random coincidences is by acquiring a delayed window. As stated previously, individual gamma-rays tagged with their detection times and a valid event are recorded when two detection events occur within a specified coincidence timing window. Interestingly, the rate of random coincidences can be estimated by purposefully pairing gamma-rays that arrive at *different*

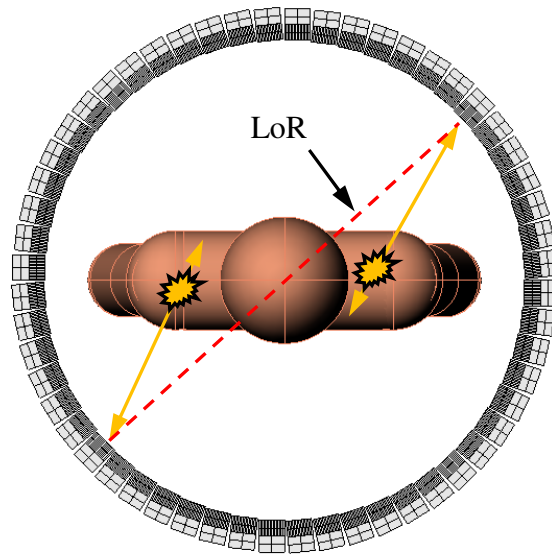


Figure 1-5: A schematic showing a Line of Response (LoR) from a random coincidence event.

times, which is practically implemented by temporally shifting the coincidence acceptance window for one of the detectors by an amount greater than the length of the window itself. The delay prevents the detection of any true gamma-ray pairs, and instead represents an estimate of the distribution of random coincidences that are unintentionally detected with coincident timing windows. The estimate of random coincidences can then be subtracted directly from the data needing to be corrected.

Since the recorded random coincidence rate is only a sample rate and not an actual account of randoms occurring in the undelayed window, the subtraction of this value does introduce some statistical noise. This uncertainty remaining after subtraction can be represented with the following,

$$\sigma_{(Trues + scatter)} = \sqrt{(Trues + Scatter) + (2 \times Randoms)}$$

where *Trues* is the number of true coincidence events, *Scatter* is the number of scattered coincidence events and the *Randoms* is the number of random coincidence events.

1.4.3 Scatter Correction

A scatter coincidence occurs when one or both annihilation gamma-rays are deflected, inside the patient or inside the scintillation crystals, from their original trajectories by Compton scattering but are nonetheless detected in time coincidence (Figure 1-6). Similarly to the presence of random coincidences, the presence of scattered coincidences compromises spatial resolution and quantitative accuracy, and results in reconstructed images with a background “haze” that is more prevalent towards the center of the FoV.

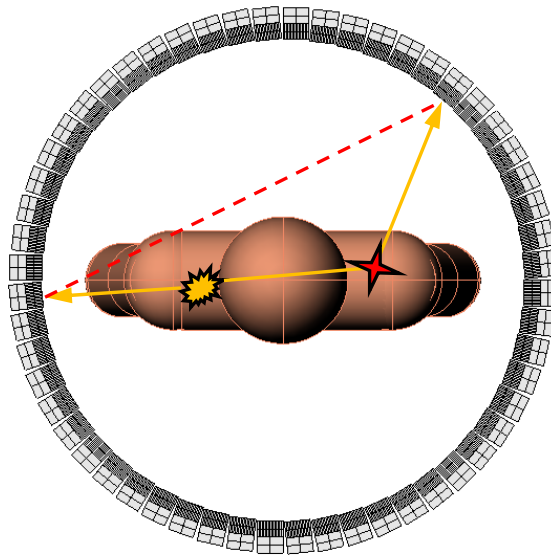


Figure 1-6: A schematic showing a Line of Response (LoR) from a scatter coincidence event.

The subject of scatter correction has received considerable attention for decades in PET physics literature. The class of scatter correction most widely implemented today is the iterative model-based scatter correction (60). Although specific implementations vary, the general methodology is as follows: the correction begins with (i) a measurement

of the projection data that includes both useful data as well as scattered data, and (ii) a measurement of the distribution of density inside the object being measured. The first step is to ignore the presence of scatter in the projection data, and perform a preliminary tomographic reconstruction. Next, a computer uses the preliminary reconstruction, the distribution of object density, and a model of photon propagation to simulate the distribution of scatter that PET scanner would have recorded, resulting in an estimate of the scatter distribution. This scatter estimate is then subtracted from the measured projection data, resulting in a slight reduction in the amount of scatter in the projection data. The process can be repeated several times, but no objective criteria for determining the optimal number of iterations has been agreed upon broadly.

1.4.4 Attenuation Correction

Attenuation is the gradual loss of signal intensity as it passes through a medium. It is an important source of error in both SPECT and PET imaging, and is observed often as a broad reduction in radiotracer concentration in the central FoV of tomographic reconstructions. Attenuation can also manifest more subtly, appearing as localized reductions in radiotracer concentrations in cardiac and liver imaging, which can adversely affect diagnostic accuracy.

As with scattered coincidences, the origin of the attenuation phenomenon lies with the physical process of Compton scatter. However, in the case of attenuation, at least one of the gamma-rays is scattered away from the PET detector rings, and is “lost”. Also, as with scatter, modern techniques for attenuation correction rely upon an estimate of the distribution of material that is causing the Compton scattering. With such an estimate in hand, one can effect an attenuation correction in a manner similar to that described earlier for scatter correction.

The accuracy of scatter and attenuation corrections is determined by both the quality of the physical models of gamma-ray propagation, as well as the quality of the density measurement of the object through which the gamma-rays are propagating. This density measurement is more specifically a measurement of the spatial distribution of linear attenuation coefficients within the FoV of the PET scanner. This is often termed a “ μ -

map”, where μ is a common symbol for linear attenuation. The estimation, or measurement, of μ -maps has seen considerable evolution since the inception of PET, with each generation of technique typically improving in spatial resolution and contrast, and decreasing in noise and acquisition time. Strategies for generating μ -maps fall into two categories: non-transmission strategies that rely solely upon the measured radiotracer distribution, and transmission strategies that rely upon an independent measurement of tissue attenuation coefficients.

1.5 Attenuation Correction Methods

1.5.1 Non-Transmission μ -maps

Non-transmission μ -maps are generated by analyzing properties of the radiotracer distribution in the projection data. Generally, the assumption is made that the observed radionuclide distribution is bounded by a single convex hull, such as an ellipse, characterized by a single uniform attenuation coefficient within its perimeter. The boundary of the ellipse can be estimated by a trained operator or an edge detection algorithm applied to the emission data.

Although relatively simple to implement and easy for an operator to use, drawing contours manually often does not result in perfect “fits” to patients, the quality of fit will vary between operators, and a uniform distribution may not account for the true heterogeneity of attenuation coefficients within a patient’s body (61).

One way to help improve consistency with a uniform mapping approach is to eliminate the inter-operator variability by automating the task of contouring with edge-detection algorithms. There have been several automated approaches based on different edge-detection algorithms. Some have made use of the Compton scattered gamma-rays to determine the convex contour of patients (62, 63), while others have estimated the patient outer contour directly from the unscattered projection data (64, 65), and one group has incorporated both (66).

1.5.2 Transmission-based μ -maps

Transmission-based μ -maps are created from direct measurements of attenuation in the body. The principal of this measurement is very similar to x-ray CT: a known flux of gamma-rays or x-rays passes through the body, is attenuated by it, and then detected on the opposite side.

1.5.2.1 Radionuclide Transmission Scans

An external radionuclide source can be used to transmit gamma-rays, of one or more discrete energy levels, through the body to map the distribution of linear attenuation coefficients at an energy of interest. These radionuclide transmission scans can be acquired before radiotracer injection (67, 68), after the injection but during the PET scan (69, 70), or after PET scan (71, 72). Each option has advantages and disadvantages.

In oncologic whole-body surveys, the region to be scanned is much longer than the axial FoV of the PET scanner. This requires the PET data to be acquired in a step-and-record manner, where the PET scanned bed moves incrementally and longitudinally through the PET scanner. For this scenario, a practical and simple to implement solution is to alternate, in an interleaved manner, transmission and PET scanning for each bed position. This however, increases patient scan time, both hindering patient throughput and patient comfort. These interleaved scans also suffer from image registration problems, due to patient motion or misalignment between scans.

Performing the transmission scan during the emission scan reduces scan times, but requires the radionuclide gamma-rays to be of a different energy than the PET scan energy (which is always 511 keV). This option results in errors in the μ -map from cross-talk between the transmission and emission scans. For example: if one chooses a transmission radionuclide with gamma-ray energy higher than 511 keV, like ^{137}Cs , which emits a 662 keV gamma-ray, then some of the transmission gamma-rays will contaminate the PET scan as they lose energy through Compton scatter. Further, if transmission scanning is performed at a different energy than 511 keV, the attenuation coefficients, which are energy-dependent, must be scaled to match their 511 keV counterparts.

1.5.2.2 X-ray CT Scans

The development of the hybrid PET/CT provided a “next generation” of attenuation correction. Compared with radionuclide transmission imaging, CT scans could be acquired much faster, and with higher spatial resolution and less noise. The penalties, however, were increased financial cost (now comprised of the cost of a PET scanner plus a CT scanner), increased ionizing radiation dose to the patient, and increased complexity to create the final μ -map.

X-ray has one endogenous contrast mechanism with which it can provide details about anatomy, which is electron density. This makes CT very useful for acquiring detailed images of bony structures, but its ability to provide details about soft-tissue is outdone by MRI. In a prospective comparison of the accuracy of MR and CT in determining the anatomic extent of disease in 40 patients, it was suggested that MRI might be the modality of choice when staging soft-tissue sarcomas. In this study, 23% of tumours observed in MR images were missed in their respective CT images (73). This limitation of soft-tissue imaging with CT, particularly in oncology applications when compared to MRI, has been consistent with the findings of other groups (74, 75).

Compared with radionuclide transmission scanning, X-ray CT imaging results in a much higher flux of photons passing through the body, resulting in a higher patient radiation dose. A typical PET scan, using 370 MBq of FDG, results in a whole body dose of approximately 6.23-10.73 mSv (76, 77). A typical whole-body CT can impart a dose of 7.22-25.95 mSv (76), depending on patient body size and CT protocol. This is considerably higher than the 0.20-0.26 mSv resulting from a radionuclide transmission scan (78). For reference, the annual background in Canada is approximately 3 mSv. For example, assuming a detriment coefficient of 5.6×10^{-5} [/mSv] (20-64 yrs of age population, References ICRP-60 and NCRP-115), the use of CT will increase the long-term risk of developing cancer by $(7.22-0.20) \times (5.6 \times 10^{-5}) \times 100\% = 0.039$. With this in mind, many groups have begun researching dose reduction strategies for X-ray CT, including variable current x-ray tubes, reconstruction algorithms that model the statistical processes of x-ray measurements, and iterative reconstruction techniques.

Both X-ray CT and some radionuclide transmission scans are acquired at different energies than a PET scan, which is always a monoenergetic 511 keV. Thus x-ray CT μ -maps, like radionuclide μ -maps, must be energy-scaled to be used for attenuation correction. However, X-ray imaging has the added complication of using a polyenergetic (and continuous) spectrum ranging from 40-140 kV (or about 40 kV with filtration) to the x-ray tube kilovoltage peak, usually set near 140 kV for a tungsten anode for PET attenuation correction. Since attenuation coefficients are energy dependent, the coefficients measured at CT energies must be converted to their respective coefficients at 511 keV before the correction factors can be calculated. At 511 keV, the majority of photon interactions for all biological materials are Compton scatter, whereas photoelectric absorption is essentially negligible. However, in the CT energy range for bones, photoelectric absorption becomes a dominate effect. To complicate this further, the attenuation coefficients of different materials do not change in the same way when photon energies change. However, there are translation algorithms, which use bilinear mapping functions to perform these corrections, and they work well fundamentally because both monoenergetic photon attenuation and polychromatic photon attenuation are related to electron density (79, 80).

1.5.2.3 PET/MRI

PET/MRI represents the hybridization of two very flexible but very different imaging modalities. Unlike the hybridization of PET and CT, or SPECT and CT; PET/MRI combines modalities that exploit the properties of ionizing radiation (PET) and non-ionizing radiation (MRI). To a large extent, aspects of this difference were what complicated and delayed the development of PET/MRI.

As described earlier, conventional PET scanners use photomultiplier tubes (PMTs) to spatially localize gamma-ray absorption in a scintillation crystal. Unfortunately, for PET/MRI, PMTs are sensitive to magnetic fields. PMTs are often wrapped in mu-metal, an alloy known for its high magnetic permeability and thus useful for shielding against static or low-frequency magnetic fields. This is to partially attenuate magnetic fields, but embedding PMTs into an MRI that generates multi-Tesla magnetic fields will still render them useless. One approach to addressing this incompatibility was to use optical fibers to

lead scintillation light outside the fringe of the magnetic field or at least outside the MRI field of view (FOV) (81-88). This not only placed the PMTs outside the high magnetic field, but also placed all metallic or magnetic PET detector parts outside the MRI FOV. This minimizes the potential for interference with the magnetic field, gradients or radiofrequencies. However, this approach degrades performance, and due to the physical space occupied by the fibers, it results in PET systems with limited axial FOV (85).

Other approaches, such as in split MRI tomographs (89), or field-cycled MRI, where the magnet is shut down during PET data acquisition (90), rely on special magnet designs where the PET detector is built in between two magnets. These usually limit magnetic field strength, which limits performance, because MRI signal increases with magnetic field strength.

Alternative designs based on compact, solid-state silicon photo sensors, called avalanche photodiodes (APDs) (91), such as the small-animal PET-MRI (85, 92, 93) and the first clinical PET/MRI (94), are not sensitive to magnetic fields (95).

Siemen's first clinical PET/MRI makes use of APDs, and incorporating them was no small feat. All hardware components and assembly are optimized for both PET and MRI detection. Efforts have been made to minimize disturbances to detection of either modality from the other. RF body coils are PET transparent. PET detectors are non-magnetic and gradient transparent, so that the linearity of the gradient fields are not distorted. The APDs need to be maintained at a stable 20°C, which is achieved with a water cooling system. All PET detector electronics are completely shielded from emitting RF signals, which may otherwise disturb the MR's RF signals. This is done with copper elements.

MRI RF coils have been optimized to be as PET transparent as possible, minimizing the amount of gamma attenuation. Rigid equipment, such as the patient table, RF spine array coil and RF head coil have been scanned in a CT to form 3-D μ -maps of each. Similarly to how a patient μ -map is calculated for PET from a patient CT, the 511keV attenuation values are generated for these MRI apparatuses. These μ -maps are each registered for the PET/MRI, linked to table position, and from that point are incorporated

into the PET reconstruction process. Other, more flexible RF coils, which do not lock into a consistent position in relation to the patient table, cannot be corrected for attenuation in the same manner. Instead, the goal of PET transparency is emphasized. To achieve maximum signal-to-noise ratio (SNR) and signal for MR, without disturbing PET image quality, specific materials, optimal geometry and assembly are used.

All of these advancements have allowed PET and MR hardware to finally be fully integrated, but one of the outstanding challenges is how to best correct for patient attenuation. This is a significant challenge because MRI signals are not related to the factor that contributes to gamma-ray attenuation, which is electron density.

MRI-based attenuation correction can be divided into three categories mapping, segmentation, and atlas-based. Mapping involves creating a mathematical function that will convert MRI voxels to linear attenuation coefficients. Although this approach has great potential, it is currently limited by the similar appearance of air and bone, and the inability to map variations in lung densities. Both of these problems are due to the lack of signal obtained from bone and lung tissues from conventional MRI pulse sequences.

In segmentation, the goal is to divide the MR images into different tissues. There are a variety of approaches to doing this but once the tissues have been classified, they are then assigned theoretical attenuation values. Although this approach gives us patient specific μ -maps and can work well with tissues or mediums with consistent attenuation coefficients, this approach does have difficulty in accounting for bone and lungs, again due to the lack of signal. It also has difficulty accounting for image truncation, which can occur if part of the patient is too far from the isocenter of the main field. Also, signal noise can often cause some misclassification or incorrect segmentation.

The third approach is the atlas-based approach. This uses previously acquired data, such as MRI and CT images, and registers them to a patient's scan to obtain a customized μ -map for that patient. This approach can overcome some of the problems associated with the two previously mentioned approaches, but critically relies on an atlas that represents the intended population.

The current implementation of MR-based attenuation correction of PET by Siemens uses a 2-Dixon MRI sequence to map water and fat.() This method has been shown to provide results similar to those of conventional attenuation correction with low-dose CT() and demonstrates the importance of accounting for these different tissues. This method however, does not account for bone and is still vulnerable to image truncation and signal noise. An atlas-based approach can overcome the problems of image truncation and signal noise, as well as incorporate attenuation values for bone. However, without a patient specific mapping what are the most important qualities to take into consideration when constructing an atlas? The current *de facto* approach used with Siemens mMR considers body fat composition to be of importance. Can body mass index be used to improve the accuracy of an atlas? Also, with the obvious anatomical differences between genders perhaps it is important to have gender specific atlases, and to what extent does accounting for these attributes play a role?

The purpose of my thesis was to develop a method for MR-based attenuation correction. Specifically, we wanted to determine the extent of which gender and body mass index (BMI) affect quantitative accuracy of atlas-based attenuation correction in PET/MRI. We compared 3 approaches to atlas construction and evaluated their performance in a general oncology population. These approaches used: Body Mass Index (BMI)-specific atlases; gender-specific atlases; and a BMI- and gender-nonspecific atlas (or fully amalgamated atlas).

References

- [1] L. Fass. Imaging and cancer: A review. *Mol. Oncol.* 2(2), pp. 115-152. 2008.
- [2] M. Atri. New technologies and directed agents for applications of cancer imaging. *J. Clin. Oncol.* 24(20), pp. 3299-3308. July 10, 2006.
- [3] B. J. Hillman. Introduction to the special issue on medical imaging in oncology. *J. Clin. Oncol.* 24(20), pp. 3223-3224. July 10, 2006.
- [4] J. P. de Torres, G. Bastarrika, J. P. Wisnivesky, A. B. Alcaide, A. Campo, L. M. Seijo, J. C. Pueyo, A. Villanueva, M. D. Lozano, U. Montes, L. Montuenga and J. J. Zulueta. Assessing the relationship between lung cancer risk and emphysema detected on low-dose CT of the chest. *CHEST Journal* 132(6), pp. 1932-1938. 2007.
- [5] T. Sarkeala, S. Heinavaara and A. Anttila. Breast cancer mortality with varying invitational policies in organised mammography. *Br. J. Cancer* 98(3), pp. 641-645. 2008.
- [6] S. Shim, K. Lee, B. Kim, E. Lee, J. Choi and M. Chung. Accuracy of integrated PET/CT using fluorodeoxyglucose for the preoperative staging of non-small cell lung cancer: A prospective comparison with standalone CT. *Radiology* 236(101), pp. 1-1019. 2005.
- [7] C. Fermé, D. Vanel, V. Ribrag and T. Girinski. Role of imaging to choose treatment: Wednesday 5 october 2005, 08: 30–10: 00. *Cancer Imaging* 5(Spec No A), pp. S113. 2005.
- [8] H. Ashamalla, S. Rafla, K. Parikh, B. Mokhtar, G. Goswami, S. Kambam, H. Abdel-Dayem, A. Guirguis, P. Ross and A. Evola. The contribution of integrated PET/CT to the evolving definition of treatment volumes in radiation treatment planning in lung cancer. *Int. J. Radiat. Oncol. Biol. Phys.* 63(4), pp. 1016-1023. 2005.
- [9] A. A. Neves and K. M. Brindle. Assessing responses to cancer therapy using molecular imaging. *Biochimica Et Biophysica Acta (BBA) - Reviews on Cancer; Genomics and Predicting Drug Sensitivity* 1766(2), pp. 242-261. 2006.
- [10] K. Brindle. New approaches for imaging tumour responses to treatment. *Nat. Rev. Cancer* 8(2), pp. 94-107. 2008.
- [11] J. Yee, G. A. Akerkar, R. K. Hung, A. M. Steinauer-Gebauer, S. D. Wall and K. R. McQuaid. Colorectal neoplasia: Performance characteristics of CT colonography for detection in 300 Patients¹. *Radiology* 219(3), pp. 685-692. 2001.
- [12] M. Hellström, M. H. Svensson and A. Lason. Extracolonic and incidental findings on CT colonography (virtual colonoscopy). *Am. J. Roentgenol.* 182(3), pp. 631-638. 2004.

- [13] T. Xiong, M. Richardson, R. Woodroffe, S. Halligan, D. Morton and R. J. Lilford. Incidental lesions found on CT colonography: Their nature and frequency. *Br. J. Radiol.* 78(925), pp. 22-29. 2005.
- [14] M. Pech, G. Wieners, F. Fischbach, S. Hengst, A. Beck, G. Warschewske, E. L. Hänninen, P. Wust and J. Ricke. Synchronous CT-guided brachytherapy in patients at risk for incomplete interstitial laser ablation of liver malignancies. *Medical Laser Application* 19(2), pp. 73-82. 2004.
- [15] J. Ricke, P. Wust, A. Stohlmann, A. Beck, C. H. Cho, M. Pech, G. Wieners, B. Spors, M. Werk, C. Rosner, E. L. Hänninen and R. Felix. CT-guided interstitial brachytherapy of liver malignancies alone or in combination with thermal ablation: Phase I-II results of a novel technique. *Int. J. Radiat. Oncol. Biol. Phys.* 58(5), pp. 1496-1505. 2004.
- [16] S. Gandhi, D. A. Iannitti, W. Mayo-Smith and D. E. Dupuy. Lipiodol-guided computed tomography for radiofrequency ablation of hepatocellular carcinoma. *Clin. Radiol.* 61(10), pp. 888-891. 2006.
- [17] R. J. Zagoria, A. D. Hawkins, P. E. Clark, M. C. Hall, B. R. Matlaga, R. B. Dyer and M. Y. Chen. Percutaneous CT-guided radiofrequency ablation of renal neoplasms: Factors influencing success. *Am. J. Roentgenol.* 183(1), pp. 201-207. 2004.
- [18] C. J. Simon and D. E. Dupuy. Percutaneous minimally invasive therapies in the treatment of bone tumors: Thermal ablation. *Semin. Musculoskelet. Radiol.* 10pp. 137-144. 2006.
- [19] K. Hayashi, H. Ina, M. Tezuka, Y. Okada and T. Irie. Local therapeutic results of computed tomography-guided transcatheter arterial chemoembolization for hepatocellular carcinoma: Results of 265 tumors in 79 patients. *Cardiovasc. Intervent. Radiol.* 30(6), pp. 1144-1155. 2007.
- [20] M. E. Heilbrun, R. J. Zagoria, A. J. Garvin, M. C. Hall, K. Krehbiel, A. Southwick and P. E. Clark. CT-guided biopsy for the diagnosis of renal tumors before treatment with percutaneous ablation. *Am. J. Roentgenol.* 188(6), pp. 1500-1505. 2007.
- [21] S. Kulkarni, A. Kulkarni, D. Roy and M. H. Thakur. Percutaneous computed tomography-guided core biopsy for the diagnosis of mediastinal masses. *Ann. Thorac. Med.* 3(1), pp. 13-17. 2008.
- [22] I. Zudaire, M. D. Lozano, M. F. Vazquez, M. J. Pajares, J. Agorreta, R. Pio, J. J. Zulueta, D. F. Yankelevitz, C. I. Henschke and L. M. Montuenga. Molecular characterization of small peripheral lung tumors based on the analysis of fine needle aspirates. *Histol. Histopathol.* 23(1), pp. 33-40. 2008.

- [23] C. D. Furtado, D. A. Aguirre, C. B. Sirlin, D. Dang, S. K. Stamato, P. Lee, F. Sani, M. A. Brown, D. L. Levin and G. Casola. Whole-body CT screening: Spectrum of findings and recommendations in 1192 Patients. *Radiology* 237(2), pp. 385-394. 2005.
- [24] A. C. Silva, H. J. Lawder, A. Hara, J. Kujak and W. Pavlicek. Innovations in CT dose reduction strategy: Application of the adaptive statistical iterative reconstruction algorithm. *Am. J. Roentgenol.* 194(1), pp. 191-199. 2010.
- [25] A. K. Hara, R. G. Paden, A. C. Silva, J. L. Kujak, H. J. Lawder and W. Pavlicek. Iterative reconstruction technique for reducing body radiation dose at CT: Feasibility study. *Am. J. Roentgenol.* 193(3), pp. 764-771. 2009.
- [26] P. Prakash, M. K. Kalra, A. K. Kambadakone, H. Pien, J. Hsieh, M. A. Blake and D. V. Sahani. Reducing abdominal CT radiation dose with adaptive statistical iterative reconstruction technique. *Invest. Radiol.* 45(4), pp. 202. 2010.
- [27] J. H. Pedersen, H. Ashraf, A. Dirksen, K. Bach, H. Hansen, P. Toennesen, H. Thorsen, J. Brodersen, B. G. Skov, M. Døssing, J. Mortensen, K. Richter, P. Clementsen and N. Seersholm. The danish randomized lung cancer CT screening trial-overall design and results of the prevalence round. *J. Thorac. Oncol.* 4(5), pp. 608-614. 2009.
- [28] R. W. M. Underberg, F. J. Lagerwaard, J. P. Cuijpers, B. J. Slotman, d. K. van Sijrnensen and S. Senan. Four-dimensional CT scans for treatment planning in stereotactic radiotherapy for stage I lung cancer. *Int. J. Radiat. Oncol. Biol. Phys.* 60(4), pp. 1283-1290. 2004.
- [29] J. Wang, S. Bai, N. Chen, F. Xu, X. Jiang, Y. Li, Q. Xu, Y. Shen, H. Zhang, Y. Gong, R. Zhong and Q. Jiang. The clinical feasibility and effect of online cone beam computer tomography-guided intensity-modulated radiotherapy for nasopharyngeal cancer. *Radiother. Oncol.* 90(2), pp. 221-227. 2009.
- [30] Y. Suh, E. Weiss, H. Zhong, M. Fatyga, J. V. Siebers and P. J. Keall. A deliverable four-dimensional intensity-modulated radiation therapy-planning method for dynamic multileaf collimator tumor tracking delivery. *Int. J. Radiat. Oncol. Biol. Phys.* 71(5), pp. 1526-1536. 2008.
- [31] M. Bhattacharyya, D. Ryan, R. Carpenter, S. Vinnicombe and C. J. Gallagher. Using MRI to plan breast-conserving surgery following neoadjuvant chemotherapy for early breast cancer. *Br. J. Cancer* 98(2), pp. 289-293. 2008.
- [32] T. L. Chenevert, L. D. Stegman, J. M. G. Taylor, P. L. Robertson, H. S. Greenberg, A. Rehemtulla and B. D. Ross. Diffusion magnetic resonance imaging: An early surrogate marker of therapeutic efficacy in brain tumors. *J. Natl. Cancer Inst.* 92(24), pp. 2029-2036. 2000.

- [33] E. Liapi, J. Geschwind, J. A. Vossen, M. Buijs, C. S. Georgiades, D. A. Bluemke and I. R. Kamel. Functional MRI evaluation of tumor response in patients with neuroendocrine hepatic metastasis treated with transcatheter arterial chemoembolization. *Am. J. Roentgenol.* 190(1), pp. 67-73. 2008.
- [34] T. Stadnik, H. Everaert, S. Makkat, R. Sacré, J. Lamote and C. Bourgain. Breast imaging. preoperative breast cancer staging: Comparison of USPIO-enhanced MR imaging and 18F-fluorodeoxyglucose (FDC) positron emission tomography (PET) imaging for axillary lymph node staging—initial findings. *Eur. Radiol.* 16(10), pp. 2153-2160. 2006.
- [35] G. J. Kelloff, J. M. Hoffman, B. Johnson, H. I. Scher, B. A. Siegel, E. Y. Cheng, B. D. Cheson, J. O'Shaughnessy, K. Z. Guyton, D. A. Mankoff, L. Shankar, S. M. Larson, C. C. Sigman, R. L. Schilsky and D. C. Sullivan. Progress and promise of FDG-PET imaging for cancer patient management and oncologic drug development. *Clin. Cancer Res.* 11(8), pp. 2785-2808. 2005.
- [36] M. Ghesani, E. G. DePuey and A. Rozanski. Role of F-18 FDG positron emission tomography (PET) in the assessment of myocardial viability. *Echocardiography* 22(2), pp. 165-177. 2005.
- [37] G. Mariani, L. Moresco, G. Viale, G. Villa, M. Bagnasco, G. Canavese, J. Buscombe, H. W. Strauss and G. Paganelli. Radioguided sentinel lymph node biopsy in breast cancer surgery. *Eur. J. Nucl. Med.* 42(8), pp. 1198-1215. 2001.
- [38] M. V. Mar, S. A. Miller, E. E. Kim and H. A. Macapinlac. Evaluation and localization of lymphatic drainage and sentinel lymph nodes in patients with head and neck melanomas by hybrid SPECT/CT lymphoscintigraphic imaging. *J. Nucl. Med. Technol.* 35(1), pp. 10-16. March 2007.
- [39] H. Lerman, G. Lievshitz, O. Zak, U. Metser, S. Schneebaum and E. Even-Sapir. Improved sentinel node identification by SPECT/CT in overweight patients with breast cancer. *Eur. J. Nucl. Med.* 48(2), pp. 201-206. February 2007.
- [40] Z. Matrai, L. Toth, T. Saeki, I. Sinkovics, M. Godeny, H. Takeuchi, M. Bidlek, A. Bartal, A. Savolt, B. Dorogi and M. Kasler. The potential role of SPECT/CT in the preoperative detection of sentinel lymph nodes in breast cancer. *Orv. Hetil.* 152(17), pp. 678-688. 2011.
- [41] Z. Han, A. Fu, H. Wang, R. Diaz, L. Geng, H. Onishko and D. E. Hallahan. Noninvasive assessment of cancer response to therapy. *Nat. Med.* 14(3), pp. 343-349. 2008.
- [42] J. Symanowski, A. Maurer, R. Naumann, N. Shah, D. Morgenstern and R. Messmann. Use of 99mTc-EC20 (a folate-targeted imaging agent) to predict response to therapy with EC145 (folate-targeted therapy) in advanced ovarian cancer. *Presented at J. Clin. Oncol.* 2010.

- [43] M. Signorelli, L. Guerra, A. Buda, M. Picchio, G. Mangili, T. Dell'Anna, S. Sironi and C. Messa. Role of the integrated FDG PET/CT in the surgical management of patients with high risk clinical early stage endometrial cancer: Detection of pelvic nodal metastases. *Gynecol. Oncol.* 115(2), pp. 231-235. 2009.
- [44] E. Even-Sapir, U. Metser, E. Mishani, G. Lievshitz, H. Lerman and I. Leibovitch. The detection of bone metastases in patients with high-risk prostate cancer: 99mTc-MDP planar bone scintigraphy, single- and multi-field-of-view SPECT, 18F-fluoride PET, and 18F-fluoride PET/CT. *Eur. J. Nucl. Med.* 47(2), pp. 287-297. February 2006.
- [45] E. Even-Sapir, E. Mishani, G. Flusser and U. Metser. 18F-fluoride positron emission tomography and positron emission tomography/computed tomography. *Presented at Seminars in Nuclear Medicine.* 2007.
- [46] R. L. Wahl, L. E. Quint, R. L. Greenough, C. R. Meyer, R. I. White and M. B. Orringer. Staging of mediastinal non-small cell lung cancer with FDG PET, CT, and fusion images: Preliminary prospective evaluation. *Radiology* 191(2), pp. 371-377. 1994.
- [47] L. Freudenberg, G. Antoch, S. Mueller, R. Goerges and A. Bockisch. Whole body FDG-PET/CT in restaging of lymphoma. *J. Nucl. Med.* 44(Suppl 5), pp. 83P. 2003.
- [48] J. van Loon, J. Grutters, R. Wanders, L. Boersma, M. Oellers, A. Dingemans, G. Bootsma, W. Geraedts, C. Pitz, J. Simons, S. Fatah, G. Snoep, M. Hochstenbag, P. Lambin and D. De Ruyscher. Follow-up with 18FDG-PET-CT after radical radiotherapy with or without chemotherapy allows the detection of potentially curable progressive disease in non-small cell lung cancer patients: A prospective study. *Eur. J. Cancer* 45(4), pp. 588-595. 2009.
- [49] T. Inoue, E. E. Kim, S. Wallace, D. J. Yang, F. C. L. Wong, P. Bassa, A. Cherif, E. Delpassand, A. Buzdar and D. A. Podoloff. Positron emission tomography using [18F] fluorotamoxifen to evaluate therapeutic responses in patients with breast cancer: Preliminary study. *Cancer Biother. Radiopharm.* 11(4), pp. 235-245. 1996.
- [50] M. Moehler, A. Dimitrakopoulou-Strauss, F. Gutzler, U. Raeth, L. G. Strauss and W. Stremmel. ¹⁸F-labeled fluorouracil positron emission tomography and the prognoses of colorectal carcinoma patients with metastases to the liver treated with 5-fluorouracil. *Cancer* 83(2), pp. 245-253. 1998.
- [51] K. A. Kurdziel, D. O. Kiesewetter, R. E. Carson, W. C. Eckelman and P. Herscovitch. Biodistribution, radiation dose estimates, and in vivo ppg modulation studies of 18F-paclitaxel in nonhuman primates. *Eur. J. Nucl. Med.* 44(8), pp. 1330-1339. 2003.

- [52] S. M. Larson, Y. Erdi, T. Akhurst, M. Mazumdar, H. A. Macapinlac, R. D. Finn, C. Casilla, M. Fazzari, N. Srivastava and H. Yeung. Tumor treatment response based on visual and quantitative changes in global tumor glycolysis using PET-FDG imaging. the visual response score and the change in total lesion glycolysis. *Clinical Positron Imaging: Official Journal of the Institute for Clinical PET* 2(3), pp. 159. 1999.
- [53] R. Bos, J. J. M. van der Hoeven, E. van der Wall, P. van der Groep, P. J. van Diest, E. F. I. Comans, U. Joshi, G. L. Semenza, O. S. Hoekstra and A. A. Lammertsma. Biologic correlates of 18fluorodeoxyglucose uptake in human breast cancer measured by positron emission tomography. *J. Clin. Oncol.* 20(2), pp. 379-387. 2002.
- [54] B. M. Burt, J. L. Humm, D. A. Kooby, O. D. Squire, S. Mastorides, S. M. Larson and Y. Fong. Using positron emission tomography with [18F] FDG to predict tumor behavior in experimental colorectal cancer. *Neoplasia (New York, NY)* 3(3), pp. 189. 2001.
- [55] C. H. Schilling, S. Schuster, B. O. Palsson and R. Heinrich. Metabolic pathway analysis: Basic concepts and scientific applications in the post-genomic era. *Biotechnol. Prog.* 15(3), pp. 296-303. 1999.
- [56] C. V. Dang, B. C. Lewis, C. Dolde, G. Dang and H. Shim. Oncogenes in tumor metabolism, tumorigenesis, and apoptosis. *J. Bioenerg. Biomembr.* 29(4), pp. 345-354. 1997.
- [57] D. Rivenzon-Segal, S. Boldin-Adamsky, D. Seger, R. Seger and H. Degani. Glycolysis and glucose transporter 1 as markers of response to hormonal therapy in breast cancer. *Int. J. Cancer* 107(2), pp. 177-182. 2003.
- [58] D. Artemov, Z. M. Bhujwala, U. Pilatus and J. D. Glickson. Two-compartment model for determination of glycolytic rates of solid tumors by in vivo ¹³C NMR spectroscopy. *NMR Biomed.* 11(8), pp. 395-404. 1998.
- [59] S. P. Mathupala, A. Rempel and P. L. Pedersen. Aberrant glycolytic metabolism of cancer cells: A remarkable coordination of genetic, transcriptional, post-translational, and mutational events that lead to a critical role for type II hexokinase. *J. Bioenerg. Biomembr.* 29(4), pp. 339-343. 1997.
- [60] H. Zaidi. Scatter modelling and correction strategies in fully 3-D PET. *Nucl. Med. Commun.* 22(11), pp. 1181. 2001.
- [61] S. A. Larsson and others. Gamma camera emission tomography. Development and properties of a multi-sectional emission computed tomography system. *Acta Radiologica.Supplementum* 363pp. 1. 1980.

- [62] Macey, DJ and DeNardo, GL and DeNardo, SJ and others. Comparison of three boundary detection methods for SPECT using compton scattered photons. *Eur. J. Nucl. Med.* 29(2), pp. 203. 1988.
- [63] R. Ben Younes, J. Mas and R. Bidet. A fully automated contour detection algorithm the preliminary step for scatter and attenuation compensation in SPECT. *Eur. J. Nucl. Med. Mol. I.* 14(12), pp. 586-589. 1988.
- [64] T. J. Hebert, S. Gopal and P. Murphy. A fully automated optimization algorithm for determining the 3-D patient contour from photo-peak projection data in SPECT. *Medical Imaging, IEEE Transactions On* 14(1), pp. 122-131. 1995.
- [65] T. Tomitani. An edge detection algorithm for attenuation correction in emission CT. *Nuclear Science, IEEE Transactions On* 34(1), pp. 309-312. 1987.
- [66] T. S. Pan, M. A. King, D. S. Luo, S. T. Dahlberg and B. J. Villegas. Estimation of attenuation maps from scatter and photopeak window single photon-emission computed tomographic images of technetium 99m-labeled sestamibi. *J. Nucl. Cardiol.* 4(1), pp. 42-51. 1997.
- [67] C. Watson, A. Schaefer, W. Luk and C. M. Kirsch. Clinical evaluation of single-photon attenuation correction for 3D whole-body PET. *Presented at Nuclear Science Symposium*, 1998.
- [68] H. Zaidi, C. Laemmli, M. Allaoua, P. Gries and D. Slosman. Optimizing attenuation correction in clinical cerebral 3D PET: Which method to use. *J. Nucl. Med.* 42, pp. P195-196. 2001.
- [69] C. H. Tung, G. Gullberg, G. Zeng, P. Christian, F. Datz and H. Morgan. Nonuniform attenuation correction using simultaneous transmission and emission converging tomography. *Nuclear Science, IEEE Transactions On* 39(4), pp. 1134-1143. 1992.
- [70] C. Watson, L. Eriksson, M. Casey, W. Jones, J. Moyers, S. Miller, J. Hamill, A. Van Lingen, B. Bendriem and R. Nutt. Design and performance of collimated coincidence point sources for simultaneous transmission measurements in 3-D PET. *Nuclear Science, IEEE Transactions On* 48(3), pp. 673-679. 2001.
- [71] P. K. Hooper, S. R. Meikle, S. Eberl and M. J. Fulham. Validation of postinjection transmission measurements for attenuation correction in neurological FDG-PET studies. *Eur. J. Nucl. Med.* 37(1), pp. 128-136. 1996.
- [72] R. Smith, J. Karp, G. Muehllehner, E. Gualtieri and F. Benard. Singles transmission scans performed post-injection for quantitative whole body PET imaging. *Nuclear Science, IEEE Transactions On* 44(3), pp. 1329-1335. 1997.
- [73] B. Demas, R. Heelan, J. Lane, R. Marcove, S. Hajdu and M. Brennan. Soft-tissue sarcomas of the extremities: Comparison of MR and CT in determining the extent of disease. *Am. J. Roentgenol.* 150(3), pp. 615-620. 1988.

- [74] E. Yuh, A. Barkovich and N. Gupta. Imaging of ependymomas: MRI and CT. *Child's Nervous System* 25(10), pp. 1203-1213. 2009.
- [75] S. Huang, C. Chien, W. Lin, F. Fang, P. Wang, C. Lui, Y. Huang, B. Hung, M. Tu and C. Chang. A comparative study of fused FDG PET/MRI, PET/CT, MRI, and CT imaging for assessing surrounding tissue invasion of advanced buccal squamous cell carcinoma. *Clin. Nucl. Med.* 36(7), pp. 518-525. 2011.
- [76] B. Huang, M. W. Law and P. Khong. Whole-body PET/CT scanning: Estimation of radiation dose and cancer Risk1. *Radiology* 251(1), pp. 166-174. April 2009.
- [77] H. M. Deloar, T. Fujiwara, M. Shidahara, T. Nakamura, H. Watabe, Y. Narita, M. Itoh, M. Miyake and S. Watanuki. Estimation of absorbed dose for 2-[F-18] fluoro-2-deoxy-D-glucose using whole-body positron emission tomography and magnetic resonance imaging. *Eur. J. Nucl. Med. Mol. I.* 25(6), pp. 565-574. 1998.
- [78] T. H. Wu, Y. H. Huang, J. J. S. Lee, S. Y. Wang, S. C. Wang, C. T. Su, L. K. Chen and T. C. Chu. Radiation exposure during transmission measurements: Comparison between CT-and germanium-based techniques with a current PET scanner. *Eur. J. Nucl. Med. Mol. I.* 31(1), pp. 38-43. 2004.
- [79] C. Burger, G. Goerres, S. Schoenes, A. Buck, A. Lonn and G. Von Schulthess. PET attenuation coefficients from CT images: Experimental evaluation of the transformation of CT into PET 511-keV attenuation coefficients. *Eur. J. Nucl. Med. Mol. I.* 29(7), pp. 922-927. 2002.
- [80] P. Kinahan, D. Townsend, T. Beyer and D. Sashin. Attenuation correction for a combined 3D PET/CT scanner. *Med. Phys.* 25pp. 2046. 1998.
- [81] Y. Shao, S. Cherry, K. Farahani, R. Slates, R. Silverman, K. Meadors, A. Bowery, S. Siegel, P. Marsden and P. Garlick. Development of a PET detector system compatible with MRI/NMR systems. *Nuclear Science, IEEE Transactions On* 44(3), pp. 1167-1171. 1997.
- [82] P. B. Garlick, P. K. Marsden, A. C. Cave, H. G. Parkes, R. Slates, Y. Shao, R. W. Silverman and S. R. Cherry. PET and NMR dual acquisition (PANDA): Applications to isolated, perfused rat hearts. *NMR Biomed.* 10(3), pp. 138-142. 1997.
- [83] Y. Shao, S. R. Cherry, K. Farahani, K. Meadors, S. Siegel, R. W. Silverman and P. K. Marsden. Simultaneous PET and MR imaging. *Phys. Med. Biol.* 42(10), pp. 1965. 1999.
- [84] P. K. Marsden, D. Strul, S. F. Keevil, S. C. R. Williams and D. Cash. Simultaneous PET and NMR. *Br. J. Radiol.* 75(suppl 9), pp. S53-S59. 2002.
- [85] C. Catana, Y. Wu, M. S. Judenhofer, J. Qi, B. J. Pichler and S. R. Cherry. Simultaneous acquisition of multislice PET and MR images: Initial results with a MR-compatible PET scanner. *Eur. J. Nucl. Med.* 47(12), pp. 1968-1976. 2006.

- [86] R. R. Raylman, S. Majewski, S. K. Lemieux, S. S. Velan, B. Kross, V. Popov, M. F. Smith, A. G. Weisenberger, C. Zorn and G. D. Marano. Simultaneous MRI and PET imaging of a rat brain. *Phys. Med. Biol.* 51(24), pp. 6371. 2006.
- [87] S. Yamamoto, K. Mazumoto and M. Senda. Development of a multi-slice dual layer MR-compatible animal PET system using DOI detectors. *J. Nucl. Med.* 48, pp. 89. 2007.
- [88] R. R. Raylman, S. Majewski, S. S. Velan, S. Lemieux, B. Kross, V. Popov, M. F. Smith and A. G. Weisenberger. Simultaneous acquisition of magnetic resonance spectroscopy (MRS) data and positron emission tomography (PET) images with a prototype MR-compatible, small animal PET imager. *J. Magn. Reson.* 186(2), pp. 305-310. 2007.
- [89] A. J. Lucas, R. C. Hawkes, P. Guerra, R. E. Ansorge, R. E. Nutt, J. C. Clark, T. D. Fryer and T. A. Carpenter. Development of a combined microPET-MR system. *Presented at Nuclear Science Symposium Conference Record*, 2006. IEEE. 2006, .
- [90] K. Gilbert, W. Handler, T. Scholl, J. Odegaard and B. Chronik. Design of field-cycled magnetic resonance systems for small animal imaging. *Phys. Med. Biol.* 51(11), pp. 2825. 2006.
- [91] R. Grazioso, N. Zhang, J. Corbeil, M. Schmand, R. Ladebeck, M. Vester, G. Schnur, W. Renz and H. Fischer. APD-based PET detector for simultaneous PET/MR imaging. *Nuclear Instruments and Methods in Physics Research Section A: Accelerators, Spectrometers, Detectors and Associated Equipment* 569(2), pp. 301-305. 2006.
- [92] M. S. Judenhofer, C. Catana, B. K. Swann, S. B. Siegel, W. I. Jung, R. E. Nutt, S. R. Cherry, C. D. Claussen and B. J. Pichler. PET/MR images acquired with a compact MR-compatible PET detector in a 7-T Magnet1. *Radiology* 244(3), pp. 807-814. 2007.
- [93] D. Schlyer, P. Vaska, C. Woody, D. Tomasi, S. Southekal, S. Solis-Najera, S. Stoll, J. Pratte, S. Junnarkar and S. Krishnamoorthy. First images from the BNL simultaneous PET/MRI scanner. *J. Nucl. Med.* 48pp. 289. 2007.
- [94] H. Schlemmer, B. Pichler, K. Wienhard, M. Schmand, C. Nahmias, D. Townsend, W. Heiss and C. Claussen. Simultaneous MR/PET for brain imaging: First patient scans. *J. Nucl. Med.* 48(suppl 2), pp. 45P. 2007.
- [95] B. J. Pichler, M. S. Judenhofer, C. Catana, J. H. Walton, M. Kneilling, R. E. Nutt, S. B. Siegel, C. D. Claussen and S. R. Cherry. Performance test of an LSO-APD detector in a 7-T MRI scanner for simultaneous PET/MRI. *Eur. J. Nucl. Med.* 47(4), pp. 639-647. 2006.

Chapter 2

2 A Comparison of Gender and BMI-based approaches to Atlas Design for Attenuation Correction in PET/MRI

2.1 Introduction

Several manufacturers have recently marketed PET/MRI scanners. Many authors speculate that this combination of powerful imaging technologies will lead to novel methods in diagnosis and therapy management over the coming years [1-3]. Combining PET and MRI is a complex endeavor, and many issues remain to be resolved. Among challenges under active investigation is how to perform PET attenuation [4-7]. Attenuation in PET is caused by gamma-rays being scattered by electrons in tissue and then failing to be detected in coincidence. Attenuation can be corrected with knowledge of the spatial distribution of electron density, which can be measured with X-ray CT [8]. This, in part, has contributed to the success of combined PET/CT. However, MRI measurements are more closely related to proton density and magnetic properties of tissues rather than electron density, and therefore not easily amenable for use in attenuation correction [7, 9, 10].

Three approaches to creating attenuation maps from MRI are: image segmentation [2, 7, 10], mapping [5, 11], and atlas map registration [12, 13]. We and others have published studies comparing the three PET/MRI attenuation correction methods under various conditions [6, 12-14].

2.1.1 Image Segmentation

Image segmentation involves partitioning a 3D image volume into discrete sub-volumes using visual quantitation, noise consideration, and a prior knowledge of morphology [14]. These sub-volumes are assigned tissue classifications and then attenuation coefficients are assigned using a lookup table of known values.

Some of the challenges associated with segmentation include an absence of bone and lung from the attenuation maps (μ -maps). This is particularly problematic in bone lesions and areas of complex air-bone interfaces, like the paranasal sinuses [2, 7]. MRI susceptibility artifacts and partial volume effects compromise accurate segmentation of small features such as the vertebral column, and objects such as the tendon connecting the lower jaw bone and the temporal muscle can often be misclassified as bone because of reduced relaxation rates [7]. Ignoring these tissues can lead to quantitative errors in PET reconstruction, although others have found no difference in clinical interpretations in methods neglecting bone [2]. These quantitative errors are often shown as underestimates of Standardized Uptake Values (SUV), which is the tissue radioactivity concentration at a particular point in time, divided by the injected dose at the time of injection per unit of body weight. It is calculated by,

$$SUV(t) = \frac{\text{tissue activity concentration}(t)}{\text{injected activity} / \text{body weight}}$$

where *tissue activity concentration* is in units such as MBq/kg, *injected activity* is in MBq, and *body weight* is in kg. Despite this, some efforts have been made to obtain MR signal from cortical bone with the addition of ultra-short echo (UTE) sequences [7].

2.1.2 Mapping

Mapping involves creating a mathematical function that will convert MRI voxels to linear attenuation coefficients based on MRI voxel intensity. This approach has the potential to be the most powerful and robust method of creating MRI-based μ -maps because it can be done without making assumptions about patient anatomy or tissue health [5, 15]. This could yield a continuous distribution of μ that spatially corresponds to the patient's individual anatomy. Unfortunately, difficulties with these approaches often stem from the appearance of bone and air being too similar to resolve by a simple histogram matching, or variations in lung densities being missed due to the lack of signal that can be obtained from conventional MRI pulse sequences [5, 15].

To address these problems with mapping areas of low signal, new sequences with shorter echo times and ultra-short echo times have been used to obtain signal from lung and bone tissue respectively. We have shown that variation in lung density between and within patients can be mapped [5] and signal can now also be obtained from cortical bone and mapped to corresponding linear attenuation coefficients from MRI. This can be done within the range of clinically acceptable errors and without any assumptions being made about patient anatomy [5, 15].

2.1.3 Atlas Map Registration

Atlas-based or registration approaches involve spatially aligning a pre-defined spatial distribution of coefficients to a measured MRI dataset. Registering a pre-defined atlas map critically relies on the selection of an atlas that can be adaptable to a patient population. These approaches have the benefit of including bone in their μ -maps and being able to easily obtain predictions outside the tomographic field of view of the MRI, as with a larger patient's arms when placed at their sides [2, 13]. Although these benefits address some of the shortcomings of a segmentation approach, areas such as the thorax and abdomen are more error prone because of the great degree of variability between patient morphologies. Using an atlas approach requires the assumption that certain sets of attenuation coefficients will be sufficient in representing all patients in a given population, and this can lead to significant errors particularly in lung and bone [12]. Also, the presence of tumors and metallic implants in the patient impacts the quantitative accuracy of the atlases [2]. Small structures can be affected by misregistrations of boundaries as well as warped non-rigid registered tissue atlases which are smoothed and thus lose spatial resolution [12].

In a patient population where differences in anatomy, disease and pathology can be significant, it is unlikely that a single atlas will provide an adequate match for all individuals [16, 17]. Further, given the heterogeneity of body sizes and shapes even in a normal healthy population, specialized atlases could provide more accurate representations.

Given such a diverse group, we hypothesized that atlas-based attenuation correction could benefit from the use of atlases specialized to the population's subgroups. Our preliminary study demonstrated that a μ -map from a gender-matched individual with the closest body volume as a fraction of the Field of View (FoV) arguably outperformed other μ -maps obtained through a segmentation or mapping approach [14]. The purpose of this experiment was to determine the extent of which body mass index (BMI) and gender impact the quantitative accuracy of an atlas-based approach to attenuation correction in PET. Here we expand upon these findings by comparing the performance of several atlas approaches with standard CT corrected PET reconstructions.

In particular, we compare three different approaches to atlas map design, where we consider the importance of Body Mass Index (BMI) and gender in generating an acceptable match for attenuation correction of PET. One approach incorporated individuals from three BMI categories (Normal, Overweight, and Obese) and both genders. We called this atlas our fully amalgamated atlas. Our second approach incorporated individuals belonging to the same BMI categories. This resulted in three atlases; normal; overweight; and obese. All three of these atlases included both genders in equal numbers. Our third approach resulted in two atlases, which included only members of the same gender in each. Both of these atlases incorporated individuals from our three considered BMI categories.

2.2 Methods

Seventeen patients (11 males, 6 females; mean age = 58.1 ± 9.1 years), from a general oncology population who had referrals for FDG-PET/CT scans were scanned in a Discovery VCT PET/CT (General Electric Medical Systems, Waukesha, Wisconsin, USA) and then subsequently scanned in a 3 Tesla Verio MRI (Siemens Medical, Erlangen, Germany). Eligible patients included those with solitary pulmonary nodule (SPN), non-small cell lung cancer, clinical stage III non-small cell lung cancer, limited disease small cell lung cancer, thyroid cancer, germ cell tumors, colorectal cancer, lymphoma and esophageal cancer. This group consisted of men and women, both with normal, overweight, and obese BMI scores. This study was approved by our institute's Health Sciences Research Ethics Board.

Patients were administered 5 MBq/Kg of FDG (to a maximum of 555 MBq) one hour prior to the PET/CT, after fasting overnight. The PET acquisition was 3D with 210 seconds per table stop, free breathing and ungated. Ordered-Subsets Expectation Maximization (OSEM)-based reconstructions were done with 2 iterations, 28 subsets. The PET images were composed of 128 x 128 matrices with pixel size of 5.47 mm × 5.47 mm and slice thickness of 3.27 mm.

The CT scans were acquired during free but shallow breathing, with 140 kVp, and 110 mAs. Reconstructions were performed with filtered back projection with a matrix size of 512 × 512 and pixel size of 1.37 mm × 1.37 mm, and slice thickness of 3.27 mm. CTs were converted into μ -maps using the manufacturer's algorithm on the PET/CT console by down sampling through voxel averaging, resulting in a 128 × 128 matrix, smoothed with a Gaussian filter (full-width half-maximum = 10 mm). Voxel values were then replaced by applying a lookup table.

The MR images were acquired during breath holds at end of passive expiration (functional residual capacity) with a 2D Turbo-FLASH sequence (TR = 786 ms, TE = 1.32 ms, 1 signal average, flip angle = 10°, and pixel bandwidth of 630 Hz/pixel). Images were composed of 256 x 256 matrices with pixel size of 1.95 mm × 1.95 mm, and axial slice thickness of 5 mm without gaps, and an anterior/posterior phase encode direction. Five table positions, each lasting 15 seconds for 36 slices, were acquired to form whole-body images.

Radiofrequency (RF) transmission was done through the body coil and received through elements of the spine array, large flex RF coils adjacent to the field of view (FOV), and the body matrix. RF shading was reduced with prescan normalization prior to each acquisition.

2.2.1 Data Preparation and Preprocessing

Images from both MRI and PET/CT, including CT-based μ -maps, for the same patient were co-registered using 3DSlicer's Fast Nonrigid B-spline registration module [18] to register the MRI dataset to the CT. This allowed us to simulate simultaneous PET/MRI data sets.

2.2.2 Atlas Construction

The converted CT-based μ -maps and the resulting MRI/CT-based μ -map data pairs were used to construct 6 atlases: averaged male atlas; an averaged female atlas; three averaged BMI-specific atlases (obese >30 , overweight 25-29.9, Normal 18.5-24.9) [21]; and a single atlas, nonspecific to gender or BMI, which we refer to as a fully amalgamated atlas.

Gender specific atlases were created by arbitrarily selecting a patient from each gender. Three male patients, one from each of the BMI categories being considered, were then registered to the arbitrarily selected male in the previous step. Registrations were done first between CT scans and the resulting transformations were then applied to the corresponding MR images from the same patients. Co-registered images from the same modalities were averaged together, creating an MRI & CT μ -map male gender-specific atlas pair. The same steps were applied to three additional female patient scans to construct a female gender-specific atlas pair.

BMI specific atlases were created by arbitrarily selecting a patient from each of the three BMI categories; normal; overweight; and obese. Three additional patients with normal BMIs, one from the same gender and two from the opposite gender of the arbitrarily selected patient with a normal BMI in the previous step were registered to the initially chosen normal-BMI patient. Registrations were done between CT scans first and the resulting transformations were then applied to the corresponding MR images from the same patients. Co-registered images from the same modalities were averaged together, creating an MRI & CT μ -map normal-BMI atlas pair. The same steps were repeated for the overweight and obese categories to construct the remaining two BMI atlas pairs.

The fully amalgamated atlas included six patients, three from each gender and two from each of the three BMI categories used. As with the previously described approaches, one patient was arbitrarily chosen and the remaining five patients were registered to them. Again, starting with the registration between CT scans and then applying the same transformations to the corresponding patient MR images. Once registered, images from the same modalities were averaged together into an amalgamated MRI & CT μ -map atlas pair.

All registrations were done with 3D Slicer's Fast Non-rigid B-spline registration module. Registrations of MRI to CT images of the same patient were done with 20 iterations, 5 grid points on the interior of the fixed image, 100 histogram bins and 50,000 spatial samples were used for Mattes Mutual Information [19] while all other parameters were set to default values. These parameters were selected by visually assessing registrations of preliminary data with various combinations of parameters, and selecting settings that consistently yielded satisfactorily aligned images. Inter-patient CT registrations during atlas construction were done with 60 iterations, a grid size of 10, 100 histogram bins, and 250,000 spatial samples. Transformations from inter-patient registrations were then applied to the corresponding MR images with the *Resample Image (BRAINS)* module in 3D Slicer [20]. Averaging of same-modality images was done with software developed in house with Matlab 2010b, to create MRI and CT-based μ -map atlas pairs.

2.2.3 Correcting for Attenuation in Patient Data with Atlases

Attenuation in each PET image was corrected using the BMI-specific and gender-specific atlases, which corresponded to the patient's BMI and gender, the fully amalgamated atlas and the corresponding CT-based μ -map in separate reconstructions (See Figure 2-1). All four PET reconstructions were performed on scans for patients not included in the construction of the atlases. This was done by registering the MRI components of each atlas pair to the patient's MRI. This registration was performed with the same method used in the inter-patient registrations during the construction of the atlas. The transformations required to align these volumes were saved in a separate file and applied to the corresponding CT μ -map components of each atlas, again using the *Resample*

Image (BRAINS) module in 3D Slicer [20]. The newly registered atlas CT μ -maps were then loaded, along with the original PET emission data, onto the GE Discovery VCT PET/CT console where reconstructions were performed in the same fashion as the originally corrected PET, only now with the registered atlas μ -maps. This was performed using ordered subset expectation maximization (OSEM) with three iterations and eight groups. Comparisons between PET reconstructions were performed across all voxels and tissue-specific regions (soft-tissue, bone, and lung).

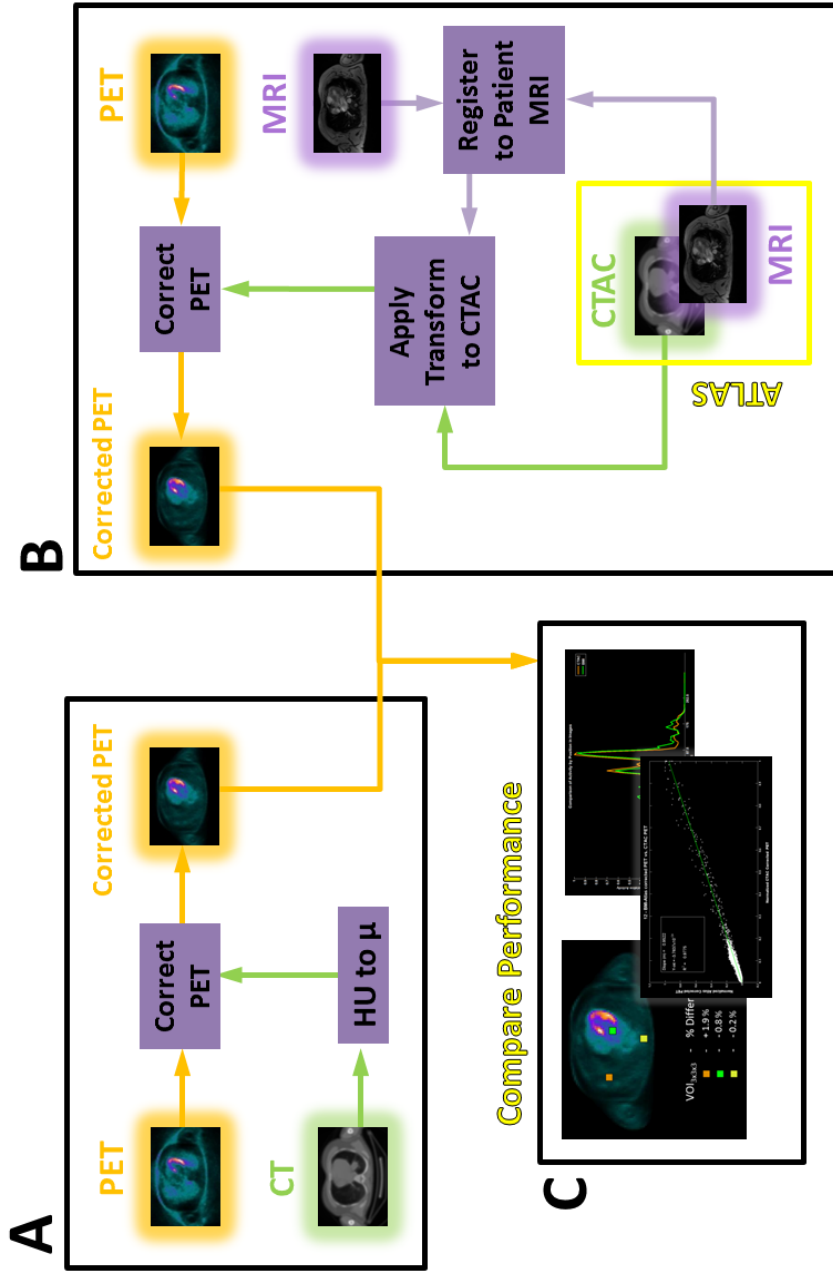


Figure 2-1: Atlas-based Reconstruction Comparison: **A)** A standard PET reconstruction for comparison. The CT image is converted into a mapping of attenuation values. This is then used to correct for the attenuation in the PET image. **B)** In our Atlas-based approach, the MRI component of the atlas is registered to the patient's MRI. The transformations used to register these MR images are then applied to the CTAC component of the Atlas. This registered CTAC is then used to correct for attenuation in the patient PET. **C)** We then compare the Atlas-based Corrected PETs to the standard CT corrected PET.

2.2.4 Data Analysis

Data analysis was performed in Matlab v7.11 (The MathWorks, MA, USA), and methodology was adapted from Marshall et al, 2011. Differences between the line integrals through PET images reconstructed with Atlas-based μ -maps and CT-based μ -maps were calculated. Least-squares regression lines of best fit (LOBFs) were calculated for scatter plots of Atlas and CT based μ -map line integrals. Measurements included LOBFs mean slope, y-intercept, correlation coefficient (R^2), and relative error. In addition to this global analysis, ten volumes of interest (VOIs) were selected to include a variety of tissues. These VOIs consisted of 3x3x3 voxels and included the caudate nucleus, cerebellum, right upper lung, aortic arch, cardiac septum, vertebral body of T8, liver, spinous process of L2, sigmoid colon, iliacus. The mean relative percent error calculated by,

$$\sum_{i=1}^n \frac{[(CT - AT) / CT] \times 100\%}{n}$$

and standard deviation for each VOI were calculated, where CT was the sum of voxel values in the VOI from the CT corrected PET image, AT was the sum of voxel values in the same VOI in the atlas corrected PET image, and n was the number of VOI being averaged together. This was calculated for all VOIs within each atlas, as well as within each atlas design approach.

2.3 Results

Examples of the two gender-based, three BMI-based, and a fully amalgamated atlas μ -map are shown in Figure 2-2. A summary of values from the global analysis through scatter plots are shown in Table 2-1, and the results from our local analysis of VOIs are shown in Figure 2-3. A detailed breakdown of each VOI for each atlas used is presented in Table 2-2.

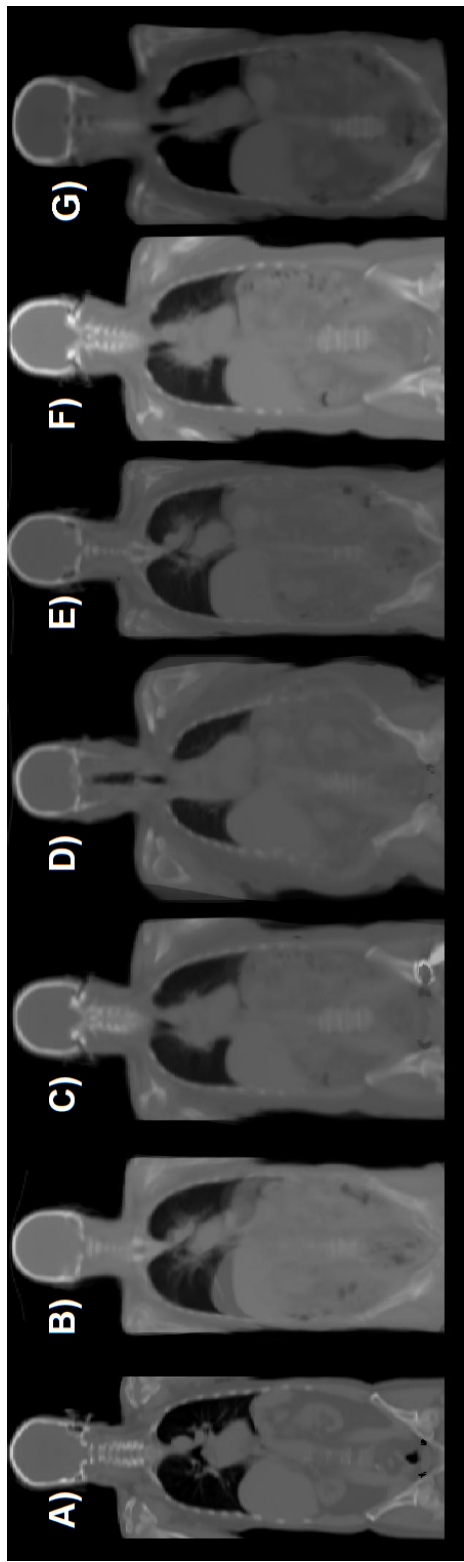


Figure 2-2: Coronal μ -map images. **A)** A single CTAC. **B)** An averaged Normal BMI atlas. **C)** An averaged overweight BMI atlas. **D)** An averaged obese BMI atlas. **E)** An averaged male atlas. **F)** An averaged female atlas. **G)** An averaged fully amalgamated atlas

PATIENT	GENDER			AMALG			BMI		
	R ²	Y-INT	SLOPE	R ²	Y-INT	SLOPE	R ²	Y-INT	SLOPE
12M	0.907	-0.001	0.929	0.917	0.004	0.915	0.899	0.006	0.900
13M	0.864	-0.001	0.890	0.904	-0.003	0.916	0.903	-0.001	0.911
14M	0.931	-0.001	0.936	0.932	0.002	0.930	0.941	-0.002	0.947
16F	0.922	0.001	0.909	0.900	0.013	0.883	0.901	0.010	0.887
17M	0.921	0.013	0.913	0.506	0.096	0.584	0.885	0.012	0.889
21F	0.914	-0.009	0.936	0.921	-0.005	0.935	0.921	-0.013	0.947
MEAN	0.910	0.000	0.919	0.847	0.018	0.861	0.908	0.002	0.913
RANK	1			3			2		

Table 2-1: Summary of parameters from LOBF in global analysis

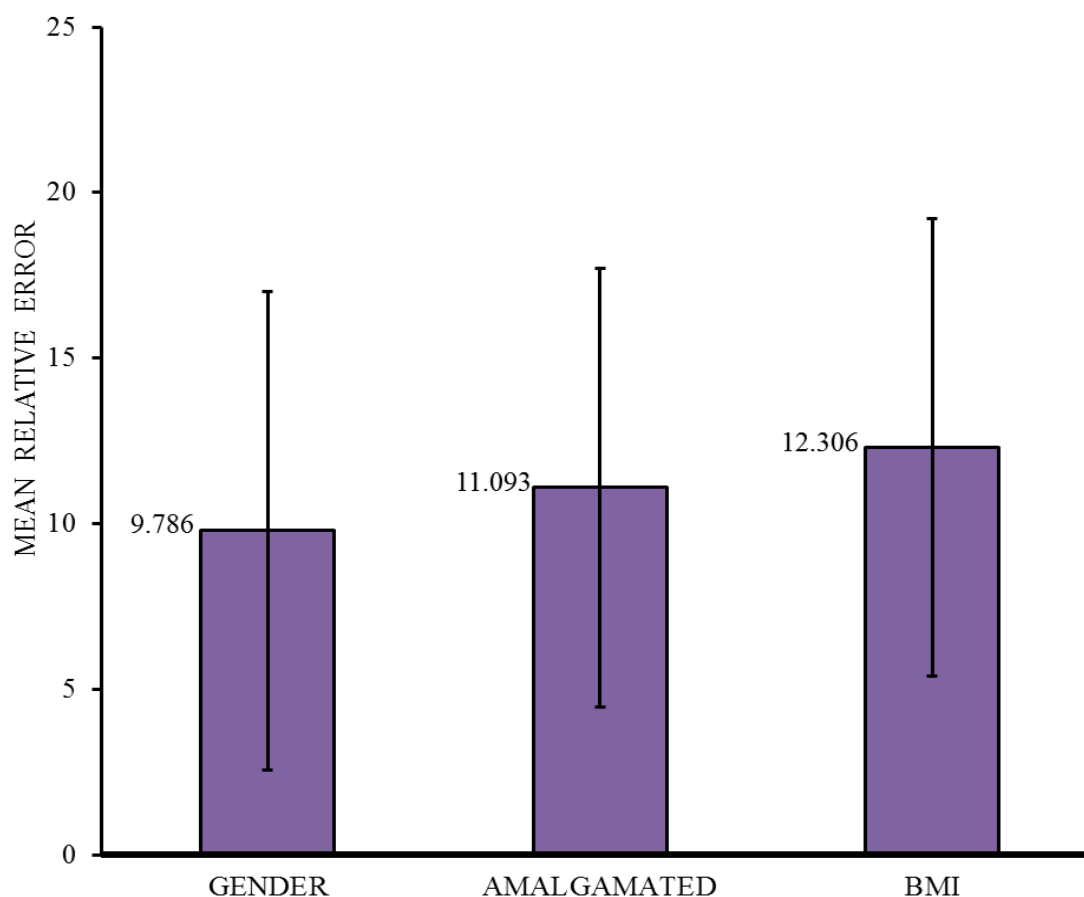


Figure 2-3: Mean relative percent error for VOIs from PET images corrected with each approach. Error bars indicating standard deviations for each category.

The results of the global analysis showed that the fully amalgamated approach to atlas design did not perform as well as the gender-based and the BMI-based approaches. The LOBFs for scatter plots comparing gender-based atlas corrected PETs with standard CT corrected PETs yielded a mean slope = 0.9190, a mean y-intercept = 0.0003, and a mean $R^2 = 0.9097$. The BMI-based atlas reconstructed PETs plotted against the standard CT corrected PETs resulted in similar results with a mean slope = 0.9133, mean y-intercept = 0.0019, and mean $R^2 = 0.9082$. The fully amalgamated atlas corrected PETs versus the standard CT corrected PETs scatter plots produced LOBFs with a mean slope = 0.8606, a mean y-intercept = 0.0178, and a mean $R^2 = 0.8465$.

Figure 2-4 shows an example of a scatter plot between an atlas corrected PET reconstruction and the corresponding CT corrected PET reconstruction. Looking towards the point of origin, we can see data points flaring out from the LOBF. These are consistent with all reconstructions, and are the result of mismatches in the lung region and related tissue boundaries. A large source of error originates from misregistration in lung tissue boundaries, particularly between the lower right lung and the liver as well as the around the mediastinum.

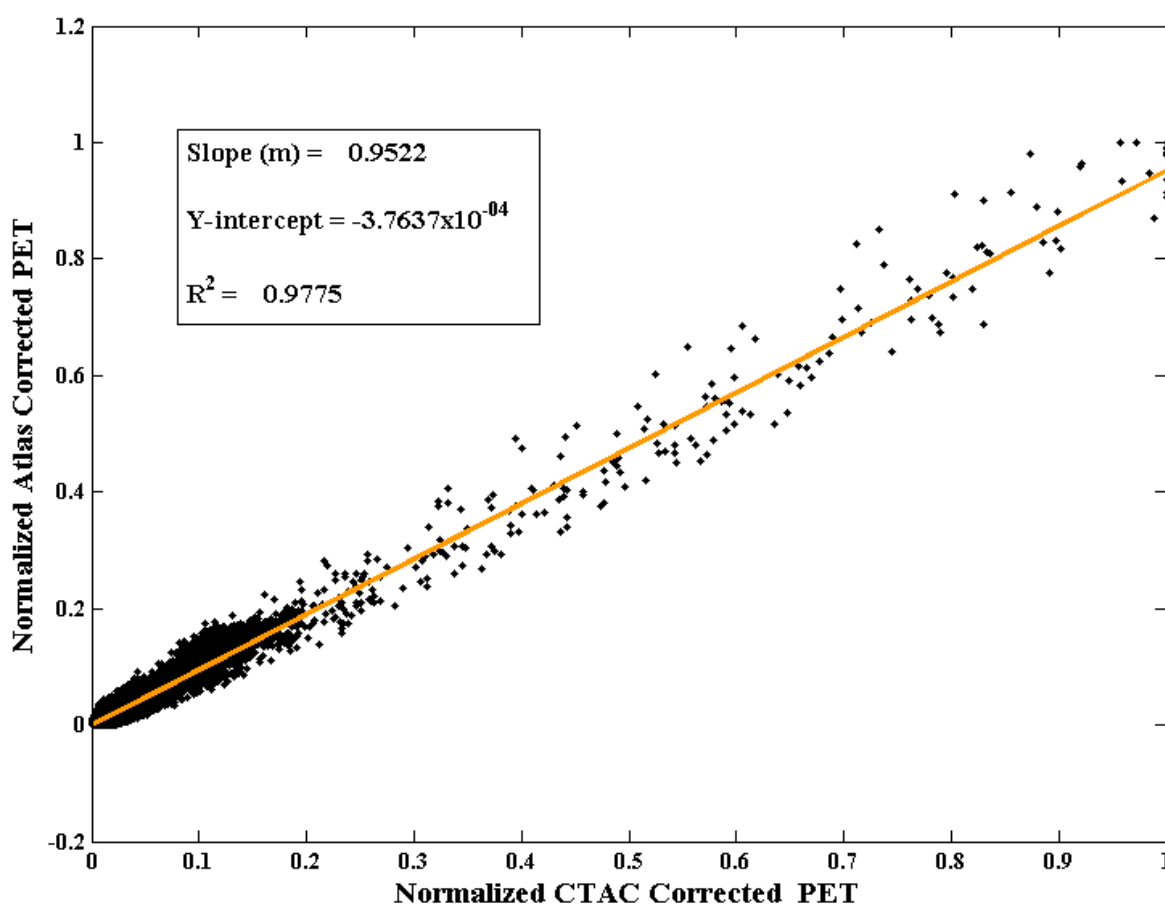


Figure 2-4: Scatter plot of Overweight BMI-based atlas corrected PET versus CTAC reconstructed PET (Patient 12)

The local analysis of 10 VOIs over the three different types of BMI-based atlas corrected PETs, two gender-based atlas corrected PETs, and the fully amalgamated atlas corrected PETs showed that the performance rankings of these methods were similar to those found in the global analysis, in that a gender-based approach consistently outperformed the other two approaches. A comparison of relative percent errors showed the gender-based corrections had a mean value = 9.786 with a standard deviation (S.D.) = 7.239, the fully amalgamated approach had a mean value = 11.093 with a S.D. = 6.636, and the BMI-based corrections mean value = 12.306 and S.D. = 6.900. A further breakdown of the atlas design approach groups into the individual atlases used, showed little difference between the BMI categories. The relative percent errors for the normal BMI category corrections had a mean value = 11.375 and S.D. = 5.673, the overweight BMI mean value = 12.761 and S.D. = 5.316, and the obese BMI mean value = 12.026 and S.D. = 5.119. However, when comparing individual gender atlases, we see that the female atlas had a noticeably lower mean relative percent error. The male atlas corrections yielded a mean relative percent error = 12.112 and S.D. = 7.725, but the female atlas corrections had a mean value = 7.702 with S.D. = 5.806. The smaller sample size in the female reconstructions may have contributed to this difference between genders.

Generally, VOIs occurring on or close to boundaries between tissues with significantly different attenuation values showed a greater relative error between atlas and original CTAC reconstructions. VOIs central to a particular tissue type showed much smaller errors. Differences between mean values for any VOIs were often as great as the differences between the design approaches themselves. The VOIs placed within soft tissues performed much better than those placed within lung or bony tissues. Two VOIs with consistently lower errors were the Caudate Nucleus and the Cerebellum. The largest errors were found in bony tissues, specifically the iliacus and the spinous process of L2. The remaining VOIs had intermediate mean error and S.D. values and were all found in soft tissues of the torso.

2.4 Registration

Accurate alignment of image data from multiple modalities is important in research, diagnosis and treatment. This process of image alignment or registration uses intensity values in the image voxels to optimize the transformations, which align the images in a three dimensional volume. Depending on the types of images being registered and the computing resources available, there are a variety of different methods and parameter settings that can be used but all are composed of a method to perform geometrical transformations to an image, a similarity metric, and an optimizer to find the best solution.

All transformations can be divided into two main categories, rigid and non-rigid. Rigid transformations maintain all relative distances between points within the same image, thus limiting all rigid transformations to rotations and translations making for 6 degrees of freedom. Non-rigid transformations include affine and b-spline transformations. Affine transformations allow for scaling and shearing in addition to rotations and translations. This gives us an additional 6 degrees of freedom, making for a total of 12 that can be used to register the images. B-spline transformations are performed by fitting complex curves through sets of control points in an image and then allowing each control point 6 degrees of freedom by translation. These complex curves are composed of polynomial curve segments. Although this method is not flexible enough for large rotations it does allow for warping, which is very useful when matching interpatient scans. In this scenario patients are always scanned in the same position, hence rotations will not be needed but variations between corresponding anatomies will require local warping.

Once a set of transformations have been applied to an image, we need a way to determine whether the transformed image is more or less similar to the target image. We perform this evaluation with a similarity metric, such as mean squared difference, normalized cross correlation, or Mattes mutual information. A mean squared difference is the sum of the squared differences between corresponding pixel values of two images divided by the product of the image dimensions. For example, we would find the mean

squared difference (MSD) of image A and image B, each of which is i pixels in the x-axis and j pixels in the y-axis by the following equation:

$$MSD = \frac{1}{ij} \sum_{x=1}^i \sum_{y=1}^j (A[x,y] - B[x,y])^2$$

However, in addition to being potentially time consuming this method is not useful for registering different modalities. Normalized cross correlation (NCC) estimates the degree of correlation between two images, where a value of 1 is a perfect correlation and a value of 0 means no correlation. This measure works particularly well for images of the same modality and is found with the following equation:

$$NCC = \frac{\sum_{x=1}^i \sum_{y=1}^j (A[x,y] - \bar{A})(B[x,y] - \bar{B})}{\left(\sqrt{\sum_{x=1}^i \sum_{y=1}^j (A[x,y] - \bar{A})^2} \right) \left(\sqrt{\sum_{x=1}^i \sum_{y=1}^j (B[x,y] - \bar{B})^2} \right)}$$

The third example of a similarity metric and the one we chose to apply to our registrations is Mattes mutual information. This metric calculates the amount of statistical dependence between two images, where the mutual information between them is maximized when the images are aligned. This metric is effective in measuring similarity between images of different modalities as well as similar modalities and can be found with the following equation:

$$MI(A, B) = H(B) - H(B|A)$$

where H is the Shannon entropy of an image. The entropy of an image can be found by using the following equation:

$$H(A) = - \sum_{\alpha} p_A(\alpha) \log p_A(\alpha)$$

where $pA(a)$ is the probability of a particular intensity value of a location within the image.

Finally, an optimizer is an algorithm used to find a global solution to our registration problem. It modifies transformation parameters and similarity metrics in order to find an optimal solution. The software package used in our study, 3D Slicer, mainly uses one-plus-one optimization and gradient-linesearch to find a best solution.

2.5 Discussion

The goal of this work was to explore the importance of gender and BMI in the quantitative accuracy of attenuation correction performed with an atlas-based μ -map in PET/MRI. We evaluated the performance of these approaches both globally and locally to identify their strengths and weaknesses. We will discuss some of the challenges faced with all of our approaches which include error-prone tissue boundaries, variable densities found in lung volumes, and similarly in bones. We will also propose some strategies to address these challenges with the current approaches.

One of the largest sources of error is related to registration rather than to the approach to atlas design. As mentioned previously, VOIs on or close to tissue boundaries were error prone and this was present amongst all of our approaches. An example of this can be seen in a plot of voxel intensity profiles in Figure 2-5a, which have been taken from the same transaxial slice through the chest of a patient's PET images reconstructed with standard CTAC in Figure 2-5b and the gender-based atlas shown in Figure 2-5c. Here we can see the profiles differing most at the boundary between the lung and liver, as well as the boundary around the mediastinum. This may in part be due to all tissues being subject to the same deformation parameters during registration. More sophisticated registration strategies that include warping penalties for more rigid structures like bone may help improve the alignment of these structures. In particular, the boundary between the lower right lung and the liver were often misaligned. This may have also been improved with a more thorough search for optimized registration parameters and similarity metrics. Thus, more work needs to be done to optimize the parameters related to registration of the atlas to patient scan.

The magnitude of the errors found within lung and bony tissues may be largely due to the variation that can be found within a population with a mean age of 60 years, as was the case with our participants. Size and density of lungs can vary considerably between patients and even among different areas within the same patient. As such, this represents an important challenge for all MRI-based approaches to attenuation correction. The variations in linear attenuation values within lung tissue are often indicative of the health or pathology present. Whether one chooses a segmentation or an atlas-based approach, the value being assigned will inevitably be a theoretical one and not necessarily reflective of the true values present within the patient. This can lead to under-correction within active lung tumors, resulting in an apparent reduction in uptake values, which may impact decisions regarding treatment.

Recently, there has been work done using lung signal obtained from short echo time MRI sequences to produce a mapping of MRI voxel intensity values to linear attenuation coefficients (96). This has the potential to provide more accurate and personalized mapping of values within the lungs of an individual patient. Incorporating this mapping technique strictly to the lung volumes within atlases could remove the majority of error and variability that occurs by providing a personalized continuous distribution of μ values, rather than the averaged distribution of μ values from a population in an atlas, or a single theoretical μ value from segmentation.

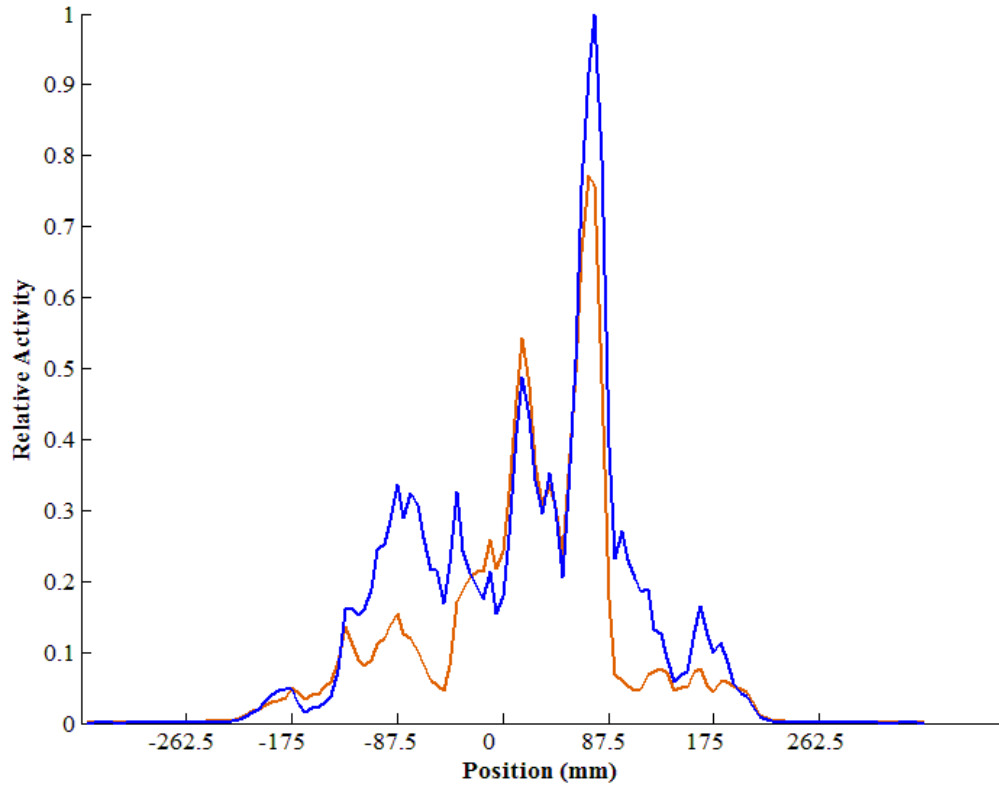


Figure 2-5a: Intensity profiles through a CTAC reconstructed PET (orange) and a Male Gender-based atlas reconstructed PET (blue) for Patient 12.

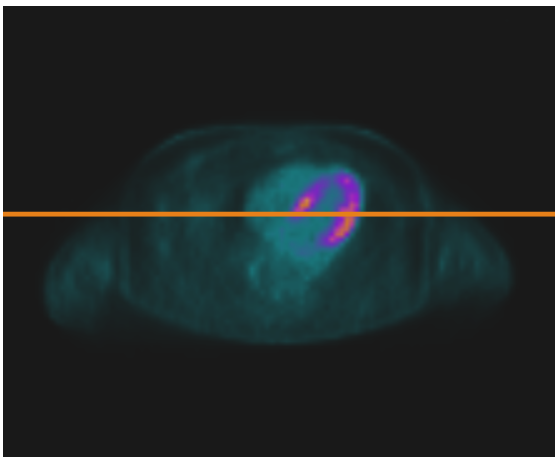


Figure 2-5b: CTAC reconstructed PET with line indicating profile plotted in Figure 4a.

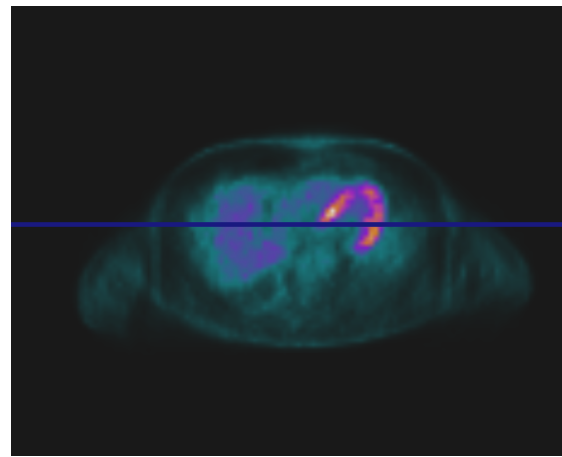


Figure 2-5c: Gender-based atlas reconstructed PET with line indicating profile plotted in Figure 4a.

Similar to the variations in density found in lung tissue, bone densities can vary greatly from patient to patient. In addition to inter-patient variations in density, bones also display a heterogeneous distribution of attenuation coefficients within the same patient. Our heterogeneous distribution of attenuation values within bones are still only representative of average bone attenuation coefficients. Our results suggest that these values cannot account for anomalies or individual differences caused by conditions, such as osteoporosis or bones lesions.

As with the short echo time sequences developed to obtain signal from lung, UTE sequence development has given rise to techniques that can obtain signal from cortical bone. Including a protocol such as this at the time of the patient scan could provide additional information for mapping underlying bone structures. Having a patient specific mapping instead of relying on an averaged representation would help improve quantitative accuracy and assessment of bone pathologies.

2.6 Conclusion

All three approaches to atlas design displayed similar error prone areas that could be improved by incorporating specialized tissue-specific MRI sequences and related mapping algorithms for lung and bone. Ultimately, it was the gender-based approach to atlas design that provided the best quantitative accuracy, both in global and local analysis.

SUMMARY OF ALL PATIENTS	AMALG_RECON		BMI_RECON		GENDER_RECON	
	SD	MEAN	SD	MEAN	SD	MEAN
Caudate Nucleus	0.532	1.148	1.148	1.401	0.382	1.035
Cerebellum	2.664	4.097	3.038	4.094	1.173	3.202
Upper Lung (Right)	12.014	14.911	9.373	18.424	6.263	7.240
Aortic Arch	13.027	17.369	9.244	13.833	11.406	14.555
Cardiac Septum	3.572	5.281	9.096	9.552	8.852	8.714
Vertebral Body of T8	6.186	8.520	5.025	9.784	11.772	18.344
Liver	7.701	12.182	5.745	14.641	6.343	11.735
Spinous Process of L2	5.941	15.355	9.901	18.187	10.237	13.957
Sigmoid Colon	3.142	7.203	5.610	11.344	9.144	12.055
Iliacus	11.130	22.295	8.946	19.280	11.347	15.582
MEAN	6.591	10.836	6.713	12.054	7.692	10.642

Table 2-2: : Mean relative percent errors and standard deviations for corrections made with each of the three atlas design methods

References

- [1] C. Catana, D. Procissi, Y. Wu, M. S. Judenhofer, J. Qi, B. J. Pichler, R. E. Jacobs and S. R. Cherry. Simultaneous in vivo positron emission tomography and magnetic resonance imaging. *Proceedings of the National Academy of Sciences* 105(10), pp. 3705-3710. 2008.
- [2] A. Martinez-Möller, M. Souvatzoglou, G. Delso, R. A. Bundschuh, C. Chefd'hotel, S. I. Ziegler, N. Navab, M. Schwaiger and S. G. Nekolla. Tissue classification as a potential approach for attenuation correction in whole-body PET/MRI: Evaluation with PET/CT data. *Eur. J. Nucl. Med.* 50(4), pp. 520-526. April 2009.
- [3] B. J. Pichler, A. Kolb, T. Nägele and H. Schlemmer. PET/MRI: Paving the way for the next generation of clinical multimodality imaging applications. *Eur. J. Nucl. Med.* 51(3), pp. 333-336. March 2010.
- [4] A. Samarin, C. Burger, S. Wollenweber, D. Crook, I. Burger, D. Schmid, G. von Schulthess and F. Kuhn. PET/MR imaging of bone lesions - implications for PET quantification from imperfect attenuation correction. *Eur. J. Nucl. Med. Mol. I.* 39(7), pp. 1154-1160. 2012.
- [5] H. R. Marshall, F. S. Prato, L. Deans, J. Théberge, R. T. Thompson and R. Z. Stodilka. Variable lung density consideration in attenuation correction of whole-body PET/MRI. *Eur. J. Nucl. Med.* 53(6), pp. 977-984. 2012.
- [6] M. Hofmann, I. Bezrukov, F. Mantlik, P. Aschoff, F. Steinke, T. Beyer, B. J. Pichler and B. Schölkopf. MRI-based attenuation correction for whole-body PET/MRI: Quantitative evaluation of segmentation- and atlas-based methods. *Eur. J. Nucl. Med.* 52(9), pp. 1392-1399. 2011.
- [7] Y. Berker, J. Franke, A. Salomon, M. Palmowski, H. C. W. Donker, Y. Temur, F. M. Mottaghy, C. Kuhl, D. Izquierdo-Garcia, Z. A. Fayad, F. Kiessling and V. Schulz. MRI-based attenuation correction for hybrid PET/MRI systems: A 4-class tissue segmentation technique using a combined ultrashort-echo-time/dixon MRI sequence. *Eur. J. Nucl. Med.* 53(5), pp. 796-804. 2012.
- [8] P. Kinahan, B. Hasegawa and T. Beyer. X-ray-based attenuation correction for positron emission tomography/computed tomography scanners. *Semin. Nucl. Med.* 33(3), pp. 166. 2003.
- [9] R. A. Pooley. Fundamental physics of MR Imaging1. *Radiographics* 25(4), pp. 1087-1099. July-August 2005.
- [10] H. R. Marshall, R. Z. Stodilka, J. Théberge, E. Sabondjian, A. Legros, L. Deans, J. M. Sykes, R. T. Thompson and F. S. Prato. A comparison of MR-based attenuation correction in PET versus SPECT. *Phys. Med. Biol.* 56(14), pp. 4613. 2011.

- [11] T. Beyer, M. Weigert, H. Quick, U. Pietrzyk, F. Vogt, C. Palm, G. Antoch, S. Müller and A. Bockisch. MR-based attenuation correction for torso-PET/MR imaging: Pitfalls in mapping MR to CT data. *Eur. J. Nucl. Med. Mol. I.* 35(6), pp. 1142-1146. 2008.
- [12] I. B. Malone, R. E. Ansorge, G. B. Williams, P. J. Nestor, T. A. Carpenter and T. D. Fryer. Attenuation correction methods suitable for brain imaging with a PET/MRI scanner: A comparison of tissue atlas and template attenuation map approaches. *Eur. J. Nucl. Med.* 52(7), pp. 1142-1149. 2011.
- [13] M. Hofmann, F. Steinke, V. Scheel, G. Charpiat, J. Farquhar, P. Aschoff, M. Brady, B. Schölkopf and B. J. Pichler. MRI-based attenuation correction for PET/MRI: A novel approach combining pattern recognition and atlas registration. *Eur. J. Nucl. Med.* 49(11), pp. 1875-1883. November 2008.
- [14] H. R. Marshall. *MRI-based attenuation correction in emission computed tomography*. PhD Thesis. The University of Western Ontario, 2012. <http://ir.lib.uwo.ca/etd/559/>
- [15] V. Keereman, Y. Fierens, T. Broux, Y. De Deene, M. Lonneux and S. Vandenberghe. MRI-based attenuation correction for PET/MRI using ultrashort echo time sequences. *Eur. J. Nucl. Med.* 51(5), pp. 812-818. May 2010.
- [16] R. Z. Stodilka, B. J. Kemp, F. S. Prato, A. Kertesz, D. Kuhl and R. L. Nicholson. Scatter and attenuation correction for brain SPECT using attenuation distributions inferred from a head atlas. *J. Nucl. Med.* 41(9), pp. 1569-1578. 2000.
- [17] M. L. Montandon and H. Zaidi. Atlas-guided non-uniform attenuation correction in cerebral 3D PET imaging. *Neuroimage* 25(1), pp. 278-286. 2005.
- [18] S. Pieper, B. Lorensen, W. Schroeder and R. Kikinis. The na-mic kit: Itk, vtk, pipelines, grids and 3d slicer as an open platform for the medical image computing community. *Presented at In Proceedings of the Third IEEE International Symposium on Biomedical Imaging*. 2006 .
- [19] D. Mattes, D. R. Haynor, H. Vesselle, T. K. Lewellyn and W. Eubank. Nonrigid multimodality image registration. *Medical Imaging*. 22(1), pp. 1609-1620. 2001.
- [20] H. Johnson, G. Harris and K. Williams. BRAINSFit: Mutual information rigid registrations of whole-brain 3D images, using the insight toolkit. *The Insight Journal*. 2007.
- [21] Canadian Guidelines for Body Weight Classification in Adults. 2003

Chapter 3

3.1 Summary

Correcting for attenuation in Positron Emission Tomography/Magnetic Resonance Imaging (PET/MRI) is difficult because there is no known relationship between MR signal and attenuation coefficients (μ) for 511 keV photons. Approaches to MRI-based attenuation correction can be divided into 3 categories; segmentation, atlas-based, and mapping.

Segmentation approaches divide an MR image into different tissue classes based on voxel intensity and location, and assign theoretical attenuation coefficients to each class, based on a look-up table. Although this approach gives us patient specific attenuation maps and can work well with tissues or mediums with consistent attenuation coefficients, this approach does have difficulty in accounting for bone and lungs (due to the lack of signal obtained from these in MRI). It also has difficulty accounting for image truncation, which can occur if part of the patient is too far from the isocenter of the main field. Also, signal noise can often cause some misclassification or incorrect segmentation.

An atlas-based approach infers a distribution of electron densities from an MRI scan using the atlas map registration approach. This relies upon spatially aligning a 3D anatomical atlas of attenuation coefficients to an MRI scan, and then using that atlas as the basis for attenuation correction of the PET scan. Unlike current segmentation approaches, a properly aligned atlas will contain a heterogeneous mapping of both lungs and bones, which may be representative of a particular population, but they may not be a precise representation of the individual. Along a similar theme, individual morphology or deviations from the population norm represented in the atlas cannot be accounted for with the current atlas methods. This being said, current atlas-based methods can provide corrections within clinically acceptable margins of error without lengthy specific MRI sequences.

Mapping involves creating a function that will convert MRI voxels to linear attenuation coefficients. Although, fundamentally, the physics behind how we achieve contrast in each modality are very different and there is no known relationship between them that could be applied across all tissues, this approach has great potential to address some of the shortcomings that are found in the other two approaches, such as making assumptions about linear attenuation coefficients and assigning uniform values to areas of inhomogeneity, or making assumptions about anatomy.

In our study, atlas corrected PET images were compared to CT corrected PET reconstructions across all voxels and tissue-specific regions. The majority of errors were more related to registration than to atlas design approach. In particular, most errors were observed in the chest area, focused around the boundary between the right lung and liver, and boundaries around the mediastinum. Further work towards optimizing registration parameters for atlas-to-patient matching is required. Ultimately, we successfully created atlas μ -maps based on matching BMI, matching gender, and a non-specific BMI or gender. All three approaches to atlas design show promise as a way to correct for attenuation in PET/MRI, based on the observed accuracy, speed, and potential applications.

3.2 Future Directions and Limitations

The current method of attenuation correction being used by Siemens in their first clinical PET/MRI uses a 2-point Dixon MRI sequence which, when segmented yield a 4-compartment (Air, Lung, Fat, Soft tissue) map [1]. This method has been evaluated in a 35 patient study and found to produce no statistically significant difference concerning anatomical localization of PET positive lesions when compared to a low-dose CT [2]. Other similar approaches have been proposed, which provide more tissue classes, such as with Hoffman et al. [3], where they use an 18 second per bed position dual-echo sequence and a 2-point Dixon method to generate fat- and water-only images and then segment into five classes; air, lungs, fat tissue, a fat-non-fat tissue mixture, and non-fat tissue. Hofmann's study showed a relative error between PET images reconstructed with CTAC and segmented MRI, for VOIs in regions of normal physiologic uptake were $14.1\% \pm 10.2\%$. This was greater than their atlas and pattern recognition approach at

7.5% \pm 7.9%, in part because the segmented approach did not include bone. When comparing the segmented MRI with the segmented CT without bone, 14.1% \pm 10.2% and 7.6% \pm 8.2% respectively, they differed by only 6.5%. A large portion of this error might be explained by the substantial increase incurred when going from the non-segmented CTAC excluding bone to the segmented CTAC excluding bone, 1.0% \pm 0.8% to 10.2% \pm 7.5% respectively. Segmentation could be increasing the amount of error by neglecting to represent the heterogeneities naturally present in patient tissues.

Although segmentation approaches perform reasonably well and will improve, they still have the shortcoming of always assigning the same theoretical value to a classified tissue type. This seems to work well with soft tissues and fat, which themselves maintain close agreement with these values, regardless of patient health. But bone and lungs do not follow the same trends. The density of lung tissue in a patient is often reflective of their lung health and there are a variety of different approaches to capturing this with MRI [4-7].

Strict approaches to MR-based attenuation correction have inherent limitations, and to date many approaches have not attempted to combine methodologies to capitalize on the strengths of one that overlap the weakness of the other. For example, perhaps better accuracy could be obtained in the thorax if the lung compartment of a segmentation approach was replaced with a mapping method capable of estimating lung density. Our group found a relationship between MRI and CT values in lung tissue was established with a 750 μ s echo-time cardiac-gated 2-dimensional turbo fast low-angle shot sequence. This demonstrated that μ -coefficients can be inferred in lung with MRI to correct for attenuation in PET, improving quantification [8].

It has been shown that for a CT energy of \sim 80keV the linear attenuation coefficient for water = 0.184 cm⁻¹ and for bone = 0.428 cm⁻¹. At the 511keV energies of PET imaging, these values are 0.096 cm⁻¹ for water and 0.172 cm⁻¹ for bone. We can see that at both energies, current approaches that classify bone as soft tissue will cause quantitative errors. Recently, work has been done to image cortical bone with MRI [9-11]. These methods do not make assumptions about patient anatomy, which make them

ideal for studies involving patient abnormalities. Whole body PET/MR images would stand to benefit from the incorporation of techniques like these, allowing for the replacement of what currently gets evaluated as soft tissue [1].

Promising results have also been shown with MRI measurements of trabecular bone with respect to osteoporosis and osteoarthritis [12, 13] and are able to improve fracture risk prediction and monitoring of osteoporosis treatment [14-17]. Incorporating these images into an MR-based attenuation map may provide us with the much needed values to correct for the most attenuating tissue in the human body, bringing us that much closer to quantitative accuracy that can contend with some of PET/MRI's predecessors. However, acquisition times for these types of images can be long and it may not be feasible to use them in most clinical scans. For example, Keereman et al's UTE approach to imaging cortical bone required a 6 minute acquisition time and Baum et al's approach to imaging cortical bone required a ~7 minute scan. This doesn't take into account any of the post processing of data that would occur to obtain the necessary information to generate attenuation values.

The atlas-based approaches we have designed for these experiments demonstrate that, within the constraints of the population they were designed for, they show promise. However, in Ontario, there are nine oncological indications (diagnostic situations or conditions) that are eligible for PET/CT, when there is sufficient evidence both that the PET scan will benefit the patient and has advantages over other testing tools (www.petscansontario.ca). These indications often show a great deal of variation between patients, with regard to location and size, among other characteristics. In a similar fashion, lung and osseous tissues can have considerable variation between patients, independent of gender and BMI. In fact, variation can also be found across similar tissues within the same patient. Again, this discrepancy between patients and heterogeneity within patients present an important challenge to any MRI-based PET attenuation correction strategy.

In developing our atlas-maps, we also considered a database approach where we registered each MRI from a collection of patient MRI/CTAC data pairs to a patient

specific MRI. The transformations from the registration with the optimal mutual information score would be used on the matching CTAC from the collection. This registered CTAC would then be used to correct for attenuation in the patient scan in the same fashion as the atlases. Again, all registrations were performed with a fast non-rigid B-spline registration with mutual information metric.

In a global analysis by linear regression of scatter plots between the database approach and standard CTAC corrected PET images, we still found the characteristic flare out of data points from the line of best fit, similar to the atlas corrected PET images. However, the database approach performed poorly overall, with the LOBFs mean slope = 0.8342, mean y-intercept = 0.00072, and $R^2 = 0.803$. This was consistent with the local analysis, where the mean relative error over the same 10 VOIs was $20.311\% \pm 14.962$, and also showing problems with tissue boundaries.

The size of the database (17 patients) appeared to be the largest contributing factor to its poor performance. Although the weighting of errors between tissue types seemed to be similar for all methods, the atlases could mitigate this through the washing out of discrepancies through the averaging that took place during atlas construction. Given a larger database with more options to find patients with more closely matched compositions, it would likely improve the performance of this method. Neither of these approaches were capable of accounting for individual variance between patients alone and ultimately will only be able to provide a closest match based on relative comparisons, instead of an absolute measure. However, with improved registration this may be sufficient for specific clinical applications.

As mentioned previously, we used Mattes mutual information as the metric for our registration of images [18]. Perhaps this final similarity score, obtained during a registration, could be used to determine whether the final atlas is suitable for attenuation correction of the patient's PET. Further work would be needed to determine a similarity threshold value for an atlas' viability, or explore other methods to measure when an atlas may not be appropriate to use. In circumstances where this threshold has been passed,

this may be an opportunity to incorporate some of the above mentioned techniques to help identify unique morphologies or signal the need for operator input.

3.3 Conclusion

This thesis has demonstrated three design approaches to atlas-based μ -maps for use in PET/MRI: averaged gender specific, averaged BMI category specific, and a fully amalgamated atlas. All three approaches showed promise as ways to correct for attenuation. The gender specific approach performed best for local and global analysis, while BMI specific atlases outperformed the amalgamated approach in global, but not local analysis. All approaches had similar error prone areas, which may indicate a limitation of the general approach and not a limitation of the design methods. Although further work to optimize registration could improve the overall performance, anatomy where inter-patient variability of attenuation coefficients play a greater role than morphology, would perhaps perform better by implementing a mapping strategy to determine patient specific densities.

References

- [1] A. Martinez-Möller, M. Souvatzoglou, G. Delso, R. A. Bundschuh, C. Chefd'hotel, S. I. Ziegler, N. Navab, M. Schwaiger and S. G. Nekolla. Tissue classification as a potential approach for attenuation correction in whole-body PET/MRI: Evaluation with PET/CT data. *Eur. J. Nucl. Med.* 50(4), pp. 520-526. April 2009.
- [2] M. Eiber, A. Martinez-Möller, M. Souvatzoglou, K. Holzapfel, A. Pickhard, D. Löffelbein, I. Santi, E. J. Rummeny, S. Ziegler and M. Schwaiger. Value of a dixon-based MR/PET attenuation correction sequence for the localization and evaluation of PET-positive lesions. *Eur. J. Nucl. Med. Mol. I.* 38(9), pp. 1691-1701. 2011.
- [3] M. Hofmann, I. Bezrukov, F. Mantlik, P. Aschoff, F. Steinke, T. Beyer, B. J. Pichler and B. Schölkopf. MRI-based attenuation correction for whole-body PET/MRI: Quantitative evaluation of segmentation- and atlas-based methods. *Eur. J. Nucl. Med.* 52(9), pp. 1392-1399. 2011.
- [4] S. B. Fain, F. R. Korosec, J. H. Holmes, R. O'Halloran, R. L. Sorkness and T. M. Grist. Functional lung imaging using hyperpolarized gas MRI. *J. Magn. Reson. Imaging* 25(5), pp. 910-923. 2007.
- [5] M. Puderbach, C. Hintze, S. Ley, M. Eichinger, H. U. Kauczor and J. Biederer. MR imaging of the chest: A practical approach at 1.5 T. *Eur. J. Radiol.* 64(3), pp. 345-355. 2007.
- [6] E. J. R. van Beek, J. M. Wild, H. U. Kauczor, W. Schreiber, J. P. Mugler and E. E. de Lange. Functional MRI of the lung using hyperpolarized 3-helium gas. *J. Magn. Reson. Imaging* 20(4), pp. 540-554. 2004.
- [7] D. A. Yablonskiy, A. L. Sukstanskii, J. C. Leawoods, D. S. Gierada, G. L. Bretthorst, S. S. Lefrak, J. D. Cooper and M. S. Conradi. Quantitative in vivo assessment of lung microstructure at the alveolar level with hyperpolarized ³He diffusion MRI. *Proceedings of the National Academy of Sciences* 99(5), pp. 3111-3116. 2002.
- [8] H. R. Marshall, R. Z. Stodilka, J. Théberge, E. Sabondjian, A. Legros, L. Deans, J. M. Sykes, R. T. Thompson and F. S. Prato. A comparison of MR-based attenuation correction in PET versus SPECT. *Phys. Med. Biol.* 56(14), pp. 4613. 2011.
- [9] V. Keereman, Y. Fierens, T. Broux, Y. De Deene, M. Lonneux and S. Vandenberghe. MRI-based attenuation correction for PET/MRI using ultrashort echo time sequences. *Eur. J. Nucl. Med.* 51(5), pp. 812-818. May 2010.
- [10] J. Du, J. C. Hermida, E. Diaz, J. Corbeil, R. Znamirovski, D. D. D'Lima and G. M. Bydder. Assessment of cortical bone with clinical and ultrashort echo time sequences. *Magn. Reson. Med.* 2012.

- [11] W. C. Bae, P. C. Chen, C. B. Chung, K. Masuda, D. D'Lima and J. Du. Quantitative ultrashort echo time (UTE) MRI of human cortical bone: Correlation with porosity and biomechanical properties. *J. Bone Miner. Res.* 27(4), pp. 848-857. 2012.
- [12] J. Marques, H. K. Genant, M. Lillholm and E. B. Dam. Diagnosis of osteoarthritis and prognosis of tibial cartilage loss by quantification of tibia trabecular bone from MRI. *Magn. Reson. Med.* 2012.
- [13] T. Baum, Y. Dütsch, D. Müller, R. Monetti, I. Sidorenko, C. R ath, E. J. Rummeny, T. M. Link and J. S. Bauer. Reproducibility of trabecular bone structure measurements of the distal radius at 1.5 and 3.0 T magnetic resonance imaging. *J. Comput. Assist. Tomogr.* 36(5), pp. 623-626. 2012.
- [14] S. L. Greenspan, S. Perera, R. Recker, J. M. Wagner, P. Greeley, B. R. Gomberg, P. Seaman and M. Kleerekoper. Changes in trabecular microarchitecture in postmenopausal women on bisphosphonate therapy. *Bone* 46(4), pp. 1006-1010. 2010.
- [15] T. Link, T. Link, T. Link, O. Saborowski, K. Kisters, M. Kempkes, M. Kosch, D. Newitt, Y. Lu and S. Waldt. Changes in calcaneal trabecular bone structure assessed with high-resolution MR imaging in patients with kidney transplantation. *Osteoporosis Int.* 13(2), pp. 119-129. 2002.
- [16] C. H. Chesnut, S. Majumdar, D. C. Newitt, A. Shields, J. Van Pelt, E. Laschansky, M. Azria, A. Kriegman, M. Olson and E. F. Eriksen. Effects of salmon calcitonin on trabecular microarchitecture as determined by magnetic resonance imaging: Results from the QUEST study. *J. Bone Miner. Res.* 20(9), pp. 1548-1561. 2005.
- [17] D. Mueller, T. Link, R. Monetti, J. Bauer, H. Boehm, V. Seifert-Klauss, E. Rummeny, G. Morfill and C. Raeth. The 3D-based scaling index algorithm: A new structure measure to analyze trabecular bone architecture in high-resolution MR images in vivo. *Osteoporosis Int.* 17(10), pp. 1483-1493. 2006.
- [18] D. Mattes, D. R. Haynor, H. Vesselle, T. K. Lewellyn and W. Eubank. Nonrigid multimodality image registration. *Medical Imaging.* 22(1), pp. 1609-1620. 2001.

Appendix A

Appendix A: Ethics Approvals

	Office of Research Ethics The University of Western Ontario Room 4180 Support Services Building, London, ON, Canada N6A 5C1 Telephone: (519) 661-3036 Fax: (519) 850-2466 Email: ethics@uwo.ca Website: www.uwo.ca/research/ethics		
	Use of Human Subjects - Ethics Approval Notice		
Principal Investigator: Dr. R.Z. Stodilka Review Number: 17253 Review Date: July 06, 2010		Review Level: Full Board Approved Local # of Participants: 15	
Protocol Title: Determination of human whole-body PET/MRI attenuation correction factors: a pilot study			
Department and Institution: Nuclear Medicine, St. Joseph's Health Care London			
Sponsor: ONT RESEARCH / CARDIOVASCULAR THERAPEUTICS			
Ethics Approval Date: August 26, 2010		Expiry Date: January 31, 2011	
Documents Reviewed and Approved: UWO Protocol (including instruments listed in Section 8.1) and Letter of Information and Consent Form dated 2010 and Release of Information Form			
Documents Received for information:			
<p>This is to notify you that The University of Western Ontario Research Ethics Board for Health Sciences Research Involving Human Subjects (HSREB) which is organized and operates according to the Tri-Council Policy Statement: Ethical Conduct of Research Involving Humans and the Health Canada/ICH Good Clinical Practice Practices: Consolidated Guidelines; and the applicable laws and regulations of Ontario has reviewed and granted approval to the above referenced study on the approval date noted above. The membership of this REB also complies with the membership requirements for REB's as defined in Division 5 of the Food and Drug Regulations.</p> <p>The ethics approval for this study shall remain valid until the expiry date noted above assuming timely and acceptable responses to the HSREB's periodic requests for surveillance and monitoring information. If you require an updated approval notice prior to that time you must request it using the UWO Updated Approval Request Form.</p> <p>During the course of the research, no deviations from, or changes to, the protocol or consent form may be initiated without prior written approval from the HSREB except when necessary to eliminate immediate hazards to the subject or when the change(s) involve only logistical or administrative aspects of the study (e.g. change of monitor, telephone number). Expedited review of minor change(s) in ongoing studies will be considered. Subjects must receive a copy of the signed information/consent documentation.</p> <p>Investigators must promptly also report to the HSREB:</p> <ul style="list-style-type: none"> a) changes increasing the risk to the participant(s) and/or affecting significantly the conduct of the study; b) all adverse and unexpected experiences or events that are both serious and unexpected; c) new information that may adversely affect the safety of the subjects or the conduct of the study. <p>If these changes/adverse events require a change to the information/consent documentation, and/or recruitment advertisement, the newly revised information/consent documentation, and/or advertisement, must be submitted to this office for approval.</p> <p>Members of the HSREB who are named as investigators in research studies, or declare a conflict of interest, do not participate in discussion related to, nor vote on, such studies when they are presented to the HSREB.</p>			
Chair of HSREB: Dr. Joseph Gilbert FDA Ref. #: IRB 0000940			
Ethics Officer to Contact for Further Information			
<input type="checkbox"/> Janice Sutherland (jsuther@uwo.ca)	<input checked="" type="checkbox"/> Elizabeth Wambolt (ewambolt@uwo.ca)	<input type="checkbox"/> Grace Kelly (grace.kelly@uwo.ca)	<input type="checkbox"/> Denise Grafton (dgrafton@uwo.ca)
This is an official document. Please retain the original in your files.			
UWO HSREB Ethics Approval - Initial V.2008-07-01 (pptApprovalNoticeHSREB_Initial)		17253	cc: ORE File LHRU Page 1 of 1

LAWSON HEALTH RESEARCH INSTITUTE**FINAL APPROVAL NOTICE**

RESEARCH OFFICE REVIEW NO.: R-10-422

PROJECT TITLE: Determination of human whole-body PET/MRI attenuation correction factors: a pilot study.

PRINCIPAL INVESTIGATOR: Dr. Rob Stodilka

DATE OF REVIEW BY CRIC: September 3, 2010

Health Sciences REB#: 17253

Please be advised that the above project was reviewed by the Clinical Research Impact Committee and the project:

Was Approved

PLEASE INFORM THE APPROPRIATE NURSING UNITS, LABORATORIES, ETC. BEFORE STARTING THIS PROTOCOL. THE RESEARCH OFFICE NUMBER MUST BE USED WHEN COMMUNICATING WITH THESE AREAS.

Dr. David Hill
V.P. Research
Lawson Health Research Institute

All future correspondence concerning this study should include the Research Office Review Number and should be directed to Sherry Paiva, CRIC Liaison, LHSC, Rm. C210, Nurses Residence, South Street Hospital.

cc: Administration

Curriculum Vitae

Name: John Christian Patrick

Post-secondary Education and Degrees: The University of Western Ontario
London, Ontario, Canada
2002-2010 B.Sc.

The University of Western Ontario
London, Ontario, Canada
2010-2012 M.Sc. candidate

Honours and Awards: First Place Oral Presentation at the University of Western Ontario
Research in Computer Science Conference (UWORCS),
2010

Canadian Institutes of Health Research Strategic Training Program
(CIHR – STP) in Vascular Research Scholarship, 2010
[\$12,000/yr]

Ontario Centres of Excellence (OCE) – Connections Program,
Project Title: *DNA probe design FISH and microarray analysis*.
2010, [\$3,230]

Western Graduate Research Scholarship (WGRS), 2011-2012,
[~\$2,500/term]

Mitacs – Accelerate Internship Program, 2012-present
[\$15,000/term]

Related Work Experience Clinical Physics Assistant
St. Joseph’s Health Care, London
2011-present

Research Assistant
Lawson Health Research Institute
2005-2011

Technical Writer
Phillips Tool & Mould Ltd.
2005-2006

Publications:

Papers Published and Submitted

HR Marshall, **J Patrick**, D Laidley, FS Prato, J Butler, J Théberge, RT Thompson, RZ Stodilka. 'To segment, register, or map? A comparison of three MRI-based attenuation correction methods for whole-body PET.' Submitted to J Nucl Med, March 19, 2012.

Robert Z. Stodilka, Julien Modolo, Frank S. Prato, John A. Robertson, Charles Cook, **John Patrick**, Anne Beuter, Alex W. Thomas, Alexandre Legros, 'Pulsed magnetic field exposure induces lasting changes in neural network dynamics', Neurocomputing Vol 74, Issues 12-13 (June, 2011)

Stodilka, R.Z., Modolo, J., Prato, F.S., Robertson, J., Cook, C., **Patrick, J.**, Beuter, A., Thomas, A.W., & A. Legros. Response of a cortical network model to long-term exposure to simple and complex stimuli. Neurocomputing (2010)

Roumeliotis, M., Ephrat, P., **Patrick, J.**, & J.J.L. Carson. Development and characterization of an omni-directional photoacoustic point source for calibration of a staring 3D photoacoustic imaging system. Opt Express 17(17): 15228-15238 (2009) - [Published | PMID: 19688001 | Free Access]

Reports

Patrick, J., Sabondjian, E, Butler, J, Théberge, J, Thompson, T, Prato, F, & Stodilka, R. NEMA Report: Acceptance testing of Siemens Biograph mMR PET/MRI., St. Joseph's Health Care London (In Progress)

Legros, A., Gow, J., McNamee, D., Corbacio, M., **Patrick, J.**, Keenlside, L., & R.Z. Stodilka. Diagnostic Assessment of Cerebral Impairment in Canadian Forces (CF) Operations – *Phase II, Milestone 2* Final Report. Lawson Health Research Institute (2008)

Presentations:

Oral

J Patrick, H Marshal, E Sabondjian, J Butler, I Rachinsky, T Thompson, J Théberge, F Prato, R Stodilka, 'The Role of Body Mass & Gender in Atlas Construction in PET/MRI', Canadian Organization of Medical Physicists (COMP) 58th Annual Scientific Meeting – Halifax, Nova Scotia, July 13, 2012.

H.R. Marshall, D.T. Laidley, MD, **J. Patrick**, BSc, J. Butler, BSc, R.T. Thompson, PhD, F. Prato, I. Rachinsky, MD, MSc, R.Z. Stodilka, PhD, 'Three MRI-based attenuation correction methods for PET.', Society of Nuclear Medicine (SNM) 2012 Annual Meeting – Miami Beach, Florida, June 9-13, 2012.

John Patrick, 'The Role of BMI & Gender in Atlas Design for PET/MRI', Medical Biophysics Departmental Talks (Western University, Canada) – London, Ontario. March 8, 2012.

John Patrick, Ben Shirley, Stephanie Dorman, Natasha Caminsky, 'FISH and aCGH Microarray Probe Design Using Ab Initio Methods', Ontario Centres of Excellence (Connections Student Presentation Forums) – London, Ontario. April 7, 2011.

John Patrick, 'Atlas-based Attenuation Correction for Whole-body PET/MRI', Medical Biophysics Departmental Talks (The University of Western Ontario) – London, Ontario. March 31, 2011.

P.K. Rogan, **J.C. Patrick**. 'Definition of Unique Sequences in Human Genome by ab initio Copy Number Determination'. SHARCNET Research Day - York University, May 6th, 2010.

Patrick J., Rogan P. 'Identifying unique sequences directly from the human genome'. UWO Research in Computer Science Conference (UWORCS) –London, Ontario. April 12th, 2010.

Stodilka, R.Z., Legros, A., Sabondjian, E., **Patrick, J.**, Robertson, J., Prato, F.S., & A.W. Thomas. 'Eliciting A Brain Model To Respond To Simple and Complex Stimuli'. BioEM 2009 Davos, Switzerland, June 14-19, 2009.

Poster

Patrick JC, Marshall H, Butler J, Rachinsky I, Thompson T, Théberge J, Prato F, Stodilka RZ. 'Atlas Construction for PET/MRI Attenuation Correction in an Oncology Population', The 9th Annual Oncology Research & Education Day – London, Ontario.

Patrick, John, Marshall, Harry R., Sabondjian, Eric, Butler, John, Theberge, Jean, Thompson, Robert T., Prato, Frank, Stodilka, Robert Z. 'Importance of gender and BMI in atlas design for PET/MRI attenuation correction', Society of Nuclear Medicine (SNM) 2012 Annual Meeting – Miami Beach, Florida. June 9-13, 2012.

D.T. Laidley, MD, H.R. Marshall, **J. Patrick**, BSc, J. Butler, BSc, F. Prato, R.T. Thompson, PhD, I. Rachinsky, MD, MSc, R.Z. Stodilka, PhD, 'Performance of PET/MRI attenuation correction in an oncology population.', Society of Nuclear Medicine (SNM) 2012 Annual Meeting – Miami Beach, Florida. June 9-13, 2012.

John Patrick, Harry Marshall, Eric Sabondjian, John Butler, Jean Theberge, Terry Thompson, Irina Rachinsky, Frank Prato, Robert Stodilka, 'BMI and Gender Dependence in Atlas Construction for Attenuation Correction in PET/MRI', London Health Research Day - London, Ontario. March 20, 2012.

Harry Marshall, Frank S. Prato, **John Patrick**, David Laidley, John Butler, Jean Theberge, R. Terry Thompson, Robert Z. Stodilka, 'To segment, to register, or to map? A comparison of three MRI-based attenuation correction methods for whole-body PET.', London Health Research Day - London, Ontario. March 20, 2012.

H. R. Marshall, D. Laidley, **J. Patrick**, J. Butler, R. T. Thompson, J. Theberge, F. S. Prato, R. Z. Stodilka, 'Attenuation correction in whole-body PET/MRI imaging', Imaging Network Ontario (ImNO) Annual Symposium - Toronto, Ontario. February 13-14, 2012.

Eric Sabondjian, **John Patrick**, Robert Z Stodilka, Martin E King, Gerald Wisenberg, Frank S Prato. 'Cardiac SPECT/CT: Comparing Slow-Rotation and Fast-Rotation CT for Attenuation Correction in Cardiac Imaging', Joint American Association of Physicists in Medicine (AAPM)/ Canadian College of Physicists in Medicine (COMP) Meeting - Vancouver, British Columbia. July 31 – August 4, 2011.

John Butler, Jodi Miller, Harry Marshall, Ali Silavi, **John Patrick**, William Pavlosky, Gregor Reid, Don Taves, Jamie Gregor, Khalil Sultan, Frank S. Prato, Terry Thompson, Rob Stodilka. 'MRI-based 3D Volumetric Serial Assessments of Physiologic Large Intestine Gas - Proof of Principle', International Society for Magnetic Resonance in Medicine 19th Annual Meeting & Exhibition – Montreal, Quebec. May 7-13, 2011.

H.R. Marshall, **J. Patrick**, R. Z. Stodilka, B. Lewden, J. Theberge, E. Sabondjian, A. Legros, A. Mitchell, L. Dorrington, J. Sykes, R. T. Thompson, and F. S. Prato. 'Attenuation correction in PET/MRI versus SPECT/MRI', Imaging Network Ontario (ImNO) Annual Symposium. – Toronto, Ontario. January 31 – February 1, 2011.

J.C. Patrick, B.C. Shirley, P.K. Rogan. 'Identifying unique sequences directly from the human genome'. The American Society of Human Genetics 60th Annual Meeting – Washington DC. November 2-6, 2010.